

CONFERENCES AND SYMPOSIA

PACS number: 01.10.Fv, 03.65.Xp, 41.20.Jb, **42.25.–p**, **43.20.+g**, 43.20.Dk, 43.20.Fn, **43.25.+y**, **43.30.+m**, **43.60.–c**, 43.60.Pt, 78.20.Ci, **78.67.–n**, 81.05.Xi, 81.05.Zx, 87.50.Y

Electromagnetic and acoustic waves in metamaterials and structures (Scientific session of the Physical Sciences Division of the Russian Academy of Sciences, 24 February 2011)

DOI: 10.3367/UFNe.0181.201111g.1201

The scientific session, titled "Electromagnetic and acoustic waves in metamaterials and structures", of the Physical Sciences Division of the Russian Academy of Sciences (RAS) was held on February 24, 2011 in the conference hall of the Lebedev Physical Institute, RAS.

The agenda of the session announced on the website www.gpad.ac.ru of the RAS Physical Sciences Division featured presentation of the following reports:

(1) **Veselago V G** (A M Prokhorov General Physics Institute, RAS, Moscow, and Moscow Institute of Physics and Technology, Dolgoprudnyi, Moscow region) "Waves in metamaterials: their role in modern physics";

(2) **Burov V A, Voloshinov V B, Dmitriev K V, Polikarpova N V** (Lomonosov Moscow State University, Moscow) "Acoustic waves in metamaterials, anisotropic crystals and anomalously refracting structures";

(3) **Shvartsburg A B** (Joint Institute for High Temperatures, RAS, Moscow), **Erokhin N S** (Space Research Institute, RAS, Moscow) "Resonant tunneling of ultrashort electromagnetic pulses in gradient metamaterials: paradoxes and prospects";

(4) **Petnikov V G** (A M Prokhorov General Physics Institute, RAS, Moscow), **Stromkov A A** (Institute of Applied Physics, RAS, Nizhny Novgorod) "Focusing of low-frequency sound fields on the ocean shelf";

(5) **Luchinin A G, Khil'ko A I** (Institute of Applied Physics, RAS, Nizhny Novgorod) "Low-mode acoustics of shallow water waveguides";

(6) **Esipov I B** (RAS Research Council on Acoustics, Moscow) "Basic results for 2010 in the field of acoustics as presented at a RAS Council session".

Papers written on the basis of these oral presentations are published below.

Uspekhi Fizicheskikh Nauk **181** (11) 1201 – 1234 (2011)
DOI: 10.3367/UFNr.0181.201111g.1201
Translated by S D Danilov, M N Sapozhnikov, and E G Strel'chenko; edited by A Radzig

PACS numbers: 41.20.Jb, **42.25.–p**, 81.05.Xi
DOI: 10.3367/UFNe.0181.201111h.1201

Waves in metamaterials: their role in modern physics

V G Veselago

The present report discusses both the already-known parameters of metamaterials and those their properties that have to date not received due research attention but which, it turns out, are fundamental for understanding some aspects of both nonrelativistic and relativistic physics.

A 'metamaterial' as currently understood is an artificial composite crystal made of macroscopic structural elements immersed in a homogeneous medium weakly absorbing electromagnetic radiation. The properties mentioned above (and to be discussed below) are those with respect to electromagnetic radiation with wavelength $\lambda > d$, where d is the characteristic crystal lattice parameter. The opposite case, $d > \lambda$, is that of so-called photonic crystals, and is not considered here.

Among other things, the reason for the interest in metamaterials is that their dielectric permittivity ε, magnetic permeability μ, and refractive index $n = \pm\sqrt{\varepsilon\mu}$ can be varied over sufficiently wide ranges by varying the size, shape, and concentration of their constituent macroscopic elements. Of particular interest is the fact that ε and μ can often be made negative, thus leading to a negative n. The electrodynamic properties of such materials with ε, μ, and $n < 0$ were described in most general terms in Ref. [1], at which time neither such materials nor indeed the term 'metamaterial' was known. Because there was no background section in that first paper, it is worthwhile to refer the reader to Fig. 1, which illustrates the logic of how the field has developed historically.

D V Sivukhin, apparently the first to point out that ε and μ can be simultaneously negative [2], was himself in doubt as to the actual existence of such materials — he did not even mention this issue in his well-known course of physics. As for Pafomov [3], his primary concern was the Cherenkov effect in

V G Veselago A M Prokhorov General Physics Institute, Russian Academy of Sciences, Moscow, Russian Federation, and the Moscow Institute of Physics and Technology, Dolgoprudnyi, Moscow region, Russian Federation. E-mail: v.veselago@relcom.ru

Uspekhi Fizicheskikh Nauk **181** (11) 1201 – 1205 (2011)
DOI: 10.3367/UFNr.0181.201111h.1201
Translated by E G Strel'chenko; edited by A Radzig

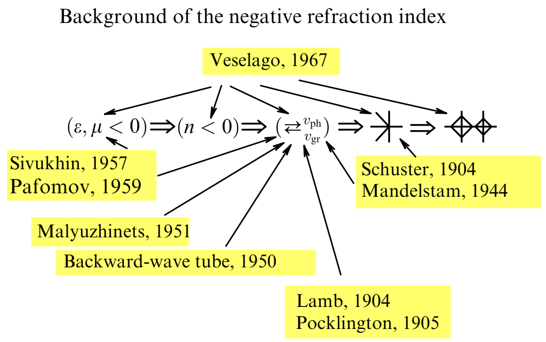

Figure 1. Short history and the development logic of introducing the concept of the negative refractive index — from negative ε and μ to a flat lens.

materials with negative ε and μ. Both Sivukhin and Pafomov argued, quite justifiably, that the phase and group velocities are antiparallel in media with negative ε and μ. Notice that, although electronic devices using such waves were already known at the time of these publications (as exemplified by long transmission lines [4] and backward-wave tubes [5]), they were, of course, not amenable in principle to a description in terms of anything like ε, μ, or n.

L I Mandelstam's lectures [6], while providing, with reference to Lamb [7], a clear physical picture of how electromagnetic waves with opposite phase and group velocities propagate in media, did not use the concepts of dielectric and magnetic permeabilities, and refractive index, let alone that of a negative refractive index. At the same time, Mandelstam discussed in detail a somewhat unconventional version of this general problem, in which a ray passes through the boundary of a medium with antiparallel group and phase velocities. In this case, the incident and refracted rays are on the same side of the interface normal. Note, though, that it was probably Schuster [8] who first pointed to this opportunity (illustrating it, parenthetically, by a schematic diagram), and that at about the same time Pocklington's work [9] was also published.

It should be noted that the very concept of a 'negative refractive index' had not been in use prior to our work [1], and that this paper was the first to trace the logical chain from negative ε and μ, to negative refractive index n, to antiparallel phase and group velocities, to the realization of Snell's law for negative n, and to a flat lens. The point to note here is that the terms 'negative refraction' and 'negative refraction index' are sometimes not distinguished from each other in the literature. The former term relates to the situation in which the refracted and incident rays are on the same side of the normal to the interface between two transparent bodies: a well-known phenomenon readily observable in, for example, transparent birefringent materials. In this case, however, referring to Snell's law

$$\frac{\sin\varphi}{\sin\phi} = n\,, \tag{1}$$

we cannot think of a universal refractive index n independent of the angle φ of incidence. It is when n is negative and independent of φ that a negative refractive index can reasonably be spoken of.

As already noted, metamaterials have offered new opportunities in the synthesis and design of new materials with novel, never-before-seen properties that can be used for very interesting and promising applications. Two such potential applications have generated a vast literature.

In the pioneering work by Pendry [10], it was shown that using a flat lens made of $n = -1$ metamaterial, superresolution imaging can be achieved, which is impossible in the limit of a geometric optics and, according to Pendry, arises here due to the propagation of so-called evanescent modes, or more precisely due to the presence of a near field.

Another major possibility that arose with the advent of metamaterials is that of creating an 'invisibility cloak', i.e. a metamaterial coating that makes the coated region invisible [11]. This possibility has already been realized and gave rise to so-called transformation optics, a field which is concerned, in effect, with changing the geometric properties of space by placing in it metamaterials with prescribed parameters [12].

Importantly, in our view, the advent of metamaterials has triggered the statement and solution of a number of fundamental problems in physics. One of these is, on the face of it, very simple: if in a negative-refraction medium the wave vector $\mathbf{k}$ is negative (because it is directed opposite to the Umov–Poynting vector $\mathbf{S}$), does it mean that the momentum of the field in such a medium will also be negative and directed opposite to the wave propagation direction which we consider to coincide with the direction of $\mathbf{S}$? Stated in more concise and simple terms, the question is: given the wave–particle duality principle, can the relation

$$p = hk \tag{2}$$

be considered valid for negative k as well? A positive answer will imply that in the absorption and reflection of waves with negative k propagating in a medium, light pressure will be replaced by light attraction. Strange as it may seem, our paper [1] was the first to address this question; a more detailed treatment was given in Ref. [13].

Most surprisingly, an even simpler question has not until recently had a clear answer: to what degree does relation (1) determine the momentum of electromagnetic radiation for positive k? Furthermore, doubts are often cast on whether the term 'electromagnetic field momentum' itself can justifiably be introduced for radiation propagating through a substance. The reason is that the field propagating through a medium sets its particles in motion (albeit on a microscopic scale), making it generally impossible, or at least difficult, to distinguish between the momentum of the field proper and that of the substance it propagates through. This point is readily interpreted by using the relativistic four-dimensional formulation to determine the forces the field exerts on the substance. For any closed system, we can introduce the energy–momentum four-dimensional tensor T_{ik} such that its four-dimensional divergence is zero:

$$\frac{\partial T_{ik}}{\partial x_k} = 0\,. \tag{3}$$

We next proceed by dividing the system into two subsystems: the electromagnetic field in some region, whose tensor T_{ik}^{f} depends only on the field strengths and inductions, E, H, D, and B, and the matter proper, with the tensor T_{ik}^{m}; we have the relationship $T_{ik} = T_{ik}^{\mathrm{f}} + T_{ik}^{\mathrm{m}}$. In that case, one can write

$$f_i = \frac{\partial T_{ik}^{\mathrm{f}}}{\partial x_k} = -\frac{\partial T_{ik}^{\mathrm{m}}}{\partial x_k}\,. \tag{4}$$

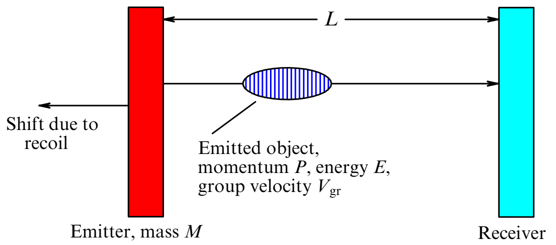

Figure 2. Schematic of how an object is ejected by the emitter and absorbed by the receiver.

Here, $f_i = \partial T^{\mathrm{f}}_{ik}/\partial x_k$ is precisely what we are looking for — the force the field exerts on the matter. Unfortunately, there is a serious problem involved in the approach being developed: it is not yet clearly understood how the tensor T^{f}_{ik} depends on field variables. The two possible forms of T^{f}_{ik} that are most often discussed were proposed by Minkowski [14] and Abraham [15] (see Appendix). The distinction between the two, which in English literature is generally identified as a 'Minkowski–Abraham controversy', consists only in the fact that the field momentum density $\mathbf{g}$ is given by $\mathbf{g} = [\mathbf{BD}]/(4\pi c)$ in the former, and by $\mathbf{g} = [\mathbf{EH}]/(4\pi c)$ in the latter. However, this seemingly small difference becomes fundamentally important when discussing forces that arise in a transparent body through which an electromagnetic wave propagates. In particular, different $\mathbf{g}$'s give rise to different magnitudes for the force that acts on the radiation absorber, and for the recoil force that acts on the field source. Estimating the latter force is key when discussing the idea proposed long ago by Einstein [16] and currently often referred to as the 'Einstein box' thought experiment. It is this thought experiment which demonstrates most clearly that the transfer of energy E in a vacuum from the emitter to the receiver involves the transfer of mass m equal to

$$m = \frac{E}{c^2}\,. \tag{5}$$

Referring to Fig. 2, the following most general considerations apply to the process in which a certain object with energy E and momentum P is transferred from the emitter to the receiver (note that the relation between the energy and momentum is not initially specified, nor is even the nature of the object transferring them discussed).

After ejecting an object with momentum P, the emitter acquires velocity

$$V = \frac{P}{M}\,, \tag{6}$$

and the object reaches the receiver in time

$$t = \frac{L}{V_{\mathrm{gr}}}\,. \tag{7}$$

In this time, the emitter shifts to the left through a distance

$$\Delta x = Vt = \frac{PL}{MV_{\mathrm{gr}}}\,. \tag{8}$$

This relation can be conveniently rewritten as

$$\Delta x M = \frac{P}{V_{\mathrm{gr}}}\,L\,. \tag{9}$$

Noting that the system as a whole has its center of inertia in the same position all the time it moves, Eqn (9) clearly implies that the mass

$$m = \frac{P}{V_{\mathrm{gr}}} \tag{10}$$

will move a distance L to the right in this time. At this point, we would do well to turn to the relation between the object's momentum P and energy E. Very importantly, this relation varies with the nature of the object. If the object is a field pulse (wave packet, photon), then the P versus E relation has the form

$$P = \frac{E}{V_{\mathrm{ph}}}\,. \tag{11}$$

This expression is a direct consequence of the particle–wave duality principle, i.e., directly follows from the relations $E = \hbar\omega$ and $P = \hbar k$. Substituting formula (11) into formula (10), we obtain

$$m = \frac{E}{V_{\mathrm{ph}} V_{\mathrm{gr}}}\,. \tag{12}$$

If the ejected object is a material body (a thrown stone, a speeding bullet, an elementary particle), then instead of formula (11) we can write (following Ref. [17])

$$P = \frac{E}{c^2}\,V_{\mathrm{gr}}\,, \tag{13}$$

which, when substituted into formula (10), yields the commonly known expression

$$m = \frac{E}{c^2}\,. \tag{14}$$

The considerations above are primarily based on the fact, seen from expressions (11) and (13), that the relation between energy and momentum is essentially different for the electromagnetic field and material particles. The reason is the Lorentz transformation: it applies to material particles, and this is exactly what ensures the validity of relation (13) and, as a consequence, of equality (14), a fundamental relation for the emitter-to-receiver mass transfer. If mass and energy are transferred by electromagnetic field, they should be taken to be related by equation (11), yielding formula (12) for the mass transfer.

For light propagation in a vacuum, when

$$V_{\mathrm{ph}} = V_{\mathrm{gr}} = c\,, \tag{15}$$

it is easily shown that both Eqn (11) and Eqn (13) yield for the mass transfer the 'standard' result, Eqn (14). Besides an electromagnetic wave in a vacuum, at least three objects can be identified for which the relation $V_{\mathrm{ph}} V_{\mathrm{gr}} = c^2$ — and, as a consequence, equality (14) — hold true:

(a) an electromagnetic wave in a plasma;

(b) an electromagnetic wave in a hollow waveguide;

(c) de Broglie waves related to the energy and momentum of material bodies by the relations $E = \hbar\omega$ and $P = \hbar k$.

Thus, it can be argued that formula (12) is the most general expression for the relation between the energy transferred and mass transferred, and that equality (14) is only its special case for $V_{\rm ph}V_{\rm gr} = c^2$. The interesting point to note is that the derivation of the well-known formula (14), which is given above and which is based on Einstein's work [16], has itself no relation whatsoever to the theory of relativity: it makes no mention of the Lorentz transformations, nor of the postulate of the threshold value of the speed of light, nor of the postulate that all physical laws are the same in all inertial reference frames. It is only on the basis of the laws of classical physics — in particular, conservation laws — that this derivation was made.

From relations (11) and (12), somewhat weird implications follow, in particular, that in the negative-index material light pressure is replaced by light attraction [1], and that the radiation transfer from the emitter to the receiver involves mass transfer in the opposite direction, from the receiver to the emitter [13]. It should be noted here that mass transfer from the emitter to the receiver (or the other way around) does not imply that the radiation itself possesses a certain mass [18].

Let us now return to the Minkowski–Abraham controversy.

The Minkowski tensor [14] can be obtained by direct calculation from Maxwell's equations, the way it is done in, for example, book [22]. In the opinion of many, the Minkowski tensor is disadvantageous because of its lack of symmetry. It is because of this fact, and because of a desire to make the tensor symmetric, that Abraham [15] changed the magnitude of field momentum g. This, though, led to the result that the tensor ceased to be covariant, as shown by direct calculation in Ref. [19], and hence of no use in calculating the forces that the field exerts on the substance in accordance with expression (4). It should be noted that the symmetry of the tensor is not itself a necessary requirement, as shown, inter alia, in Møller's book [20].

In the books [20, 22], the components of the Minkowski tensor are presented in the form of functions of **E**, **H**, **D**, and **B**. They can, however, be expressed in an equivalent form in terms of the energy density W and the components of the four-dimensional wave vector $K_i = (\mathbf{k}, \omega/c)$ and the four-dimensional group velocity

$$U_k = \left(\frac{\mathbf{u}}{\sqrt{1 - u^2/c^2}} \, , \, \frac{c}{\sqrt{1 - u^2/c^2}} \right),$$

leading to the result for the components T_{ik} in the form [21]

$$T_{ik} = \frac{W}{\omega} \sqrt{1 - \frac{u^2}{c^2}} K_i U_k \, . \tag{16}$$

Taking into account that the momentum density $g_\alpha = T_{\alpha 4}/c$, from the last formula follows that W and $\mathbf{g}$ are related by

$$g_\alpha = \frac{W k_\alpha}{\omega} \, , \tag{17}$$

which, apart from the notation, is equivalent to formula (11).

As for the Abraham tensor, the requirement that it be symmetric leads, notably, to the equality

$$g = \frac{S}{c^2} \, , \tag{18}$$

which, in turn, implies, bearing in mind the well-known relation $S = WV_{\rm gr}$, that

$$g = \frac{WV_{\rm gr}}{c^2} \, , \tag{19}$$

in complete equivalence to formula (13).

To summarize, then, the definition of the Minkowski tensor treats the momentum of the field as that of a wave, whereas for the Abraham tensor this is, in fact, the momentum of a material particle.

One further comment is in order on the Abraham tensor or, more specifically, on its spatial components. These are, in fact, identical to those of the Minkowski tensor. On the other hand, each spatial component — say, indexed by ik — equals the product of momentum density in the ith direction and the kth component of the group velocity or, in other words, to the flux of the ith component of momentum in the kth direction. It is clear that if the Minkowski and Abraham momentum densities differ, so should the spatial components of these two tensors. This is actually not the case, and it is precisely this fact which deprives the Abraham tensor of relativistic invariance. It may well be that having changed the temporal components of the tensor, Abraham just 'forgot' to change the spatial ones.

We would claim that the above discussion of the Minkowski–Abraham controversy is totally in favor of the Minkowski tensor.

In conclusion, the following points serve to summarize:

(1) The mass transferred from the emitter to the receiver by an electromagnetic field in a substance is given by

$$m = \frac{E}{V_{\rm ph} V_{\rm gr}} \, .$$

The formula $E = mc^2$ is a special case of the above relation.

(2) Inside a negative refraction material, light pressure is replaced by light attraction, and mass is transferred by light, not from the emitter to the receiver, but the other way round, from the receiver to the emitter.

(3) The Abraham tensor is not relativistically covariant and cannot generally be used to calculate forces exerted by the force on matter. For this purpose, the Minkowski tensor should be applied.

Appendix

The energy–momentum tensor can be written out in the most general form as

$$T_{ik} = \begin{bmatrix} T_{\alpha\beta} & -\mathrm{i}c\mathbf{g} \\ -\dfrac{\mathrm{i}}{c}\mathbf{S} & W \end{bmatrix} . \tag{20}$$

Here, $T_{\alpha\beta}$ are the spatial components of the tensor, with $\alpha, \beta = x, y, z$; $\mathbf{g}$ is the field momentum density; $\mathbf{S}$ is the Umov–Poynting vector, and W is the field energy density.

The individual components of the Minkowski energy–momentum tensor take the form

$$T_{\alpha\beta} = \frac{1}{4\pi} (E_\alpha D_\beta + H_\alpha B_\beta) - \frac{1}{8\pi} \, \delta_{\alpha\beta} (\mathbf{ED} + \mathbf{HB}) \, ,$$

$$\mathbf{S} = \frac{c}{4\pi} \, [\mathbf{EH}] \, , \qquad \mathbf{g} = \frac{1}{4\pi c} \, [\mathbf{DB}] \, , \qquad W = \frac{1}{8\pi} (\mathbf{ED} + \mathbf{HB}) \, .$$

The same components of the Abraham tensor are as follows:

$$T_{\alpha\beta} = \frac{1}{8\pi}(E_\alpha D_\beta + E_\beta D_\alpha + H_\alpha B_\beta + H_\beta B_\alpha) - \frac{1}{8\pi}\delta_{\alpha\beta}(\mathbf{ED} + \mathbf{HB}),$$

$$\mathbf{S} = \frac{c}{4\pi}[\mathbf{EH}], \quad \mathbf{g} = \frac{1}{4\pi c}[\mathbf{EH}], \quad W = \frac{1}{8\pi}(\mathbf{ED} + \mathbf{HB}).$$

The formula for the energy density W given above can be written out as $W = (1/8\pi)(\varepsilon E^2 + \mu H^2)$, but using this form implies that the two permeabilities ε and μ are both essentially positive. If ε and μ are negative, Ref. [23] gives the following expression for the energy density:

$$W = \frac{1}{8\pi}\left[\frac{\partial(\varepsilon\omega)}{\partial\omega}E^2 + \frac{\partial(\mu\omega)}{\partial\omega}H^2\right]. \tag{21}$$

References

1. Veselago V G *Usp. Fiz. Nauk* **92** 517 (1967) [*Sov. Phys. Usp.* **10** 509 (1968)]
2. Sivukhin D V *Opt. Spektrosk.* **3** 308 (1957)
3. Pafomov V E *Zh. Eksp. Teor. Fiz.* **36** 1853 (1959) [*Sov. Phys. JETP* **9** 1321 (1959)]
4. Malyuzhinets G D *Zh. Tekh. Fiz.* **21** 940 (1951)
5. Lebedev I V *Tekhnika i Pribory SVCh* (Microwave Technology and Instruments) Vol. 2, 2nd ed. (Moscow: Vysshaya Shkola, 1972)
6. Mandelstam L I *Zh. Eksp. Teor. Fiz.* **15** 475 (1945); *Polnoe Sobranie Trudov* (Complete Collection of Works) Vol. 2 (Ed. M A Leontovich) (Moscow: Izd. AN SSSR, 1947) p. 334; *Polnoe Sobranie Trudov* (Complete Collection of Works) Vol. 5 (Ed. M A Leontovich) (Moscow: Izd. AN SSSR, 1950) p. 419
7. Lamb H *Proc. London Math. Soc.* **1** 473 (1904)
8. Schuster A *An Introduction to the Theory of Optics* (London: Edward Arnold and Co., 1928) [Translated into Russian (Leningrad–Moscow: ONTI, 1935)]
9. Pocklington H C *Nature* **71** 607 (1905)
10. Pendry J B *Phys. Rev. Lett.* **85** 3966 (2000)
11. Pendry J B, Schurig D, Smith D R *Science* **312** 1780 (2006)
12. Kildishev A V, Shalaev V M *Usp. Fiz. Nauk* **181** 59 (2011) [*Phys. Usp.* **54** 53 (2011)]
13. Veselago V G *Usp. Fiz. Nauk* **179** 689 (2009) [*Phys. Usp.* **52** 649 (2009)]
14. Minkowski H *Göttingen Nachr.* 53 (1908); *Math. Ann.* **68** 472 (1910)
15. Abraham M *Palermo Rend.* **28** 1 (1909); *Palermo Rend.* **30** 33 (1910)
16. Einstein A *Ann. Physik* **20** 627 (1906) [Translated into Russian: *Sobranie Nauchnykh Trudov* (Collection of Scientific Works) Vol. 1 (Moscow: Nauka, 1965) p. 39]
17. Landau L D, Lifshitz E M *Teoriya Polya* (The Classical Theory of Fields) (Moscow: Nauka, 1973) p. 43 [Translated into English (Oxford: Pergamon Press, 1983)]
18. Okun' L B *Usp. Fiz. Nauk* **170** 1366 (2000) [*Phys. Usp.* **43** 1270 (2000)]
19. Veselago V G, Shchavlev V V *Usp. Fiz. Nauk* **180** 331 (2010) [*Phys. Usp.* **53** 317 (2010)]
20. Møller C *The Theory of Relativity* (Oxford: Clarendon Press, 1972) [Translated into Russian (Moscow: Atomizdat, 1975) p. 145]
21. Polevoi V G, Rytov S M *Usp. Fiz. Nauk* **125** 549 (1978) [*Sov. Phys. Usp.* **21** 630 (1978)]
22. Ugarov V A *Spetsial'naya Teoriya Otnositel'nosti* (Special Theory of Relativity) (Moscow: Nauka, 1977)
23. Landau L D, Lifshitz E M *Elektrodinamika Sploshnykh Sred* (Electrodynamics of Continuous Media) (Moscow: Nauka, 1982) p. 382 [Translated into English (Oxford: Pergamon Press, 1984)]

PACS numbers: 43.20.Dk, 43.20.Fn, 78.20.Ci, 81.05.Zx
DOI: 10.3367/UFNe.0181.201111i.1205

Acoustic waves in metamaterials, crystals, and anomalously refracting structures

V A Burov, V B Voloshinov,
K V Dmitriev, N V Polikarpova

1. Introduction

At present, much attention in the literature is being paid to media in which the propagation of waves occurs in the 'unusual' fashion. In particular, such media include so-called left-handed media in electrodynamics. The concept of these media was first proposed in paper [1], where they were introduced as media in which both the permittivity ε and permeability μ are negative. Interest in such media was rekindled after the publication of a number of papers (for example, Ref. [2]) reporting their experimental realization based on metamaterials — artificial structures with characteristic sizes of elements that are well below the wavelength of propagating radiation.

One of the unusual peculiarities of the propagation of plane waves in such media is that the Umov–Poynting vector is antiparallel to the wave vector [1]. This specific feature of the wave propagation is of a general character and is inherent in metamaterials studied not only in electrodynamics and optics, but also in acoustics. Because the phase and group velocity vectors of bulk waves in metamaterials are antiparallel, it is interesting to analyze the possibility of other spatial orientations of these vectors. It is also important to know the angles between the phase and group velocity vectors of a plane wave that can appear whatsoever in optical and acoustic anisotropic materials.

2. Double negative acoustic media

It has been shown in a number of theoretical and experimental papers [3–6] that double negative media (below, for brevity, we will call them simply negative) with negative effective dynamic characteristics (density ρ and compressibility η) are suited for playing the role of media in acoustics in which wave processes proceed similarly to those in left-handed media in electrodynamics. The characteristics of these media are dynamic in the sense that each element of such a medium within a certain frequency band can behave as an element of a homogeneous medium with negative parameters (for example, due to the presence of resonance structures in it).

In negative media, both in electrodynamics and acoustics, negative refraction can be observed, which is often described by using the wave equation or Helmholtz equation [7]. In this case, a principal difficulty appears because these equations contain the square of the refractive index, and to determine its sign, it is necessary to invoke additional considerations which can be based on the choice of one branch or another of the

V A Burov, V B Voloshinov, K V Dmitriev, N V Polikarpova
Physics Department, Lomonosov Moscow State University, Moscow, Russian Federation. E-mails: burov@phys.msu.ru, volosh@phys.msu.ru

Uspekhi Fizicheskikh Nauk **181** (11) 1205 – 1211 (2011)
DOI: 10.3367/UFNr.0181.201111i.1205
Translated by M N Sapozhnikov; edited by A Radzig

square root, on the causality principle, etc. For this reason, it was proposed to use first-order equations for describing processes in negative media [3]. In electrodynamics, these are Maxwell's equations, while in acoustics, these are the linearized hydrodynamic equations

$$\frac{\partial}{\partial t}(\hat{\eta} p) + \nabla \mathbf{v} = \varphi\,, \qquad \frac{\partial}{\partial t}(\hat{\rho} \mathbf{v}) + \nabla p = \mathbf{f}\,, \tag{1}$$

where p is the acoustic pressure, $\mathbf{v}$ is the vibrational velocity, and φ and $\mathbf{f}$ are scalar and vector primary acoustic-field sources, respectively. In the absence of dispersion, the parameters $\hat{\rho}$ and $\hat{\eta}$ are scalars; otherwise, they can be treated as time-convolution type integral operators. These parameters enter equations (1) separately, and therefore no problems appear with the choice of one sign or another.

An arbitrary distribution of parameters $\rho(\mathbf{r})$ and $\eta(\mathbf{r})$ can be represented as a sum of constant positive background values ρ_0 and η_0 with arbitrarily large additions $\rho'(\mathbf{r})$ and $\eta'(\mathbf{r})$: $\rho(\mathbf{r}) \equiv \rho_0 + \rho'(\mathbf{r})$, $\eta(\mathbf{r}) \equiv \eta_0 + \eta'(\mathbf{r})$. In the monochromatic case, system of equations (1) for the time dependence of fields fitted by $\sim \exp(-\mathrm{i}\omega t)$ can be represented in the form of the matrix analogue of the Lippmann–Schwinger equation [3]:

$$\breve{u}(\mathbf{r}) = \breve{u}_0(\mathbf{r}) + \int \hat{G}(\mathbf{r}-\mathbf{r}')\left[\hat{A}_1(\mathbf{r}')\,\breve{u}(\mathbf{r}')\right]\mathrm{d}\mathbf{r}'\,, \tag{2}$$

where $\breve{u}_0$ and $\breve{u}$ are column vectors characterizing the incident and perturbed fields, viz.

$$\breve{u}_0 \equiv \begin{pmatrix} \mathbf{v}_0 \\ p_0 \end{pmatrix}, \qquad \breve{u} \equiv \begin{pmatrix} \mathbf{v} \\ p \end{pmatrix},$$

$\hat{A}_1$ is the addition operator defined as

$$\hat{A}_1 \equiv \begin{pmatrix} \mathrm{i}\omega\rho'(\mathbf{r}) & \mathbf{0} \\ \mathbf{0} & \mathrm{i}\omega\eta'(\mathbf{r}) \end{pmatrix},$$

and $\hat{G}(\mathbf{r}-\mathbf{r}')$ is the matrix Green function expressed in terms of the Green function $G(\mathbf{r}-\mathbf{r}')$ in the Helmholtz equation:

$$\hat{G}(\mathbf{r}-\mathbf{r}') \equiv \begin{pmatrix} \mathrm{i}\omega\eta_0 & \nabla \\ \nabla & \mathrm{i}\omega\rho_0 \end{pmatrix} G(\mathbf{r}-\mathbf{r}')\,.$$

Equation (2) can be solved numerically for any configuration of the incident field $\breve{u}_0$ and arbitrary medium density and compressibility distributions.

To observe negative refraction phenomenon, we simulated the incidence of a plane monochromatic wave with the wavelength λ_0 at an angle of 18° to the normal on a rectangular plate made of a negative-index material with the parameters $\rho = -\rho_0$ and $\eta = -\eta_0$ (Fig. 1). The beam in the plate lies on the same side of the normal to its boundaries as beams in the environment. The wave fronts prove to be mirror-symmetric with respect to the plate boundaries. These properties demonstrate the negative refraction of sound in this plate. In this case, the phase velocity in the plate is directed antiparallel to the phase velocity in the environment (background medium), thereby being negative. Because the energy flux is continuous and waves are not reflected from plate boundaries, the energy flux in the system under study is oriented in the positive direction.

The following fact is noteworthy. At two points located in the environment on both sides of the plate in a straight line perpendicular to its boundaries and separated by a distance equal to the doubled thickness of the plate, the wave phases are coincident with each other (for example, points A and B in Fig. 1). This is the consequence of the phase velocity negativity in the negative medium, i.e., the phase incursion in the positive environment is exactly compensated by the phase incursion in the negative medium of the plate. This circumstance may lead to the conclusion that the causality principle is violated in negative media, and therefore they cannot exist in reality, which was discussed, for example, in review [8].

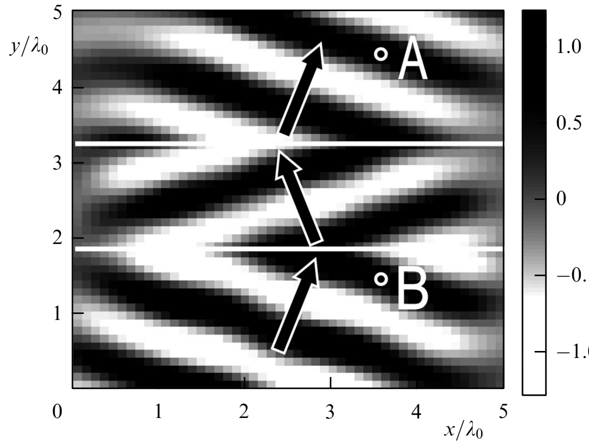

Figure 1. Real part of the calculated acoustic pressure field $p(\mathbf{r})$ during the incidence of a plane monochromatic wave on a negative-material plate. The plate boundaries are indicated by light horizontal straight lines. The arrows show the propagation directions of the wave energy in the plate and environment.

Because the discussion of the causality in the purely monochromatic case is impossible, we analyzed the following situation: nine monochromatic beams with the Gaussian amplitude distribution in the front plane are incident on a $3\,\lambda_0$-thick plate $10\,\lambda_0$ in length at an angle of 18° to the normal. The field frequency ω in the beam was varied from $\omega_0 = 2\pi c_0/\lambda_0$ to $1.4\omega_0$ in increments of $0.05\omega_0$, where $c_0 = 1/\sqrt{\rho_0\eta_0}$ is the speed of sound in the environment. The amplitudes of the beams on the axis were different and described by a Gaussian distribution over ω:

$$P(\omega) = P_0 \exp\left(-\frac{(\omega - 1.2\omega_0)^2}{(\Delta\omega)^2}\right),$$

where $\Delta\omega \approx \omega_0/6.3$. The fields calculated for each frequency were then summed up. As a result, by solving several monochromatic problems, we obtained the solution to a polychromatic problem corresponding to the propagation of an infinite series of pulses through a plate made of a negative material.

The results of calculations for a fixed instant of time are presented in Fig. 2. At the moment when the incident pulse is located at a distance equal to the plate thickness from the plate boundary, a perturbation representing a pair of pulses appears on the opposite boundary. One of the pulses continues to propagate in the environment behind the plate in the direction parallel to that of the incident pulse. Another pulse, which is mirror-symmetric to it with respect to the plate boundary, moves to the mirror-symmetric side. This pulse reaches the plate boundary simultaneously with the incident pulse, and they quench each other.

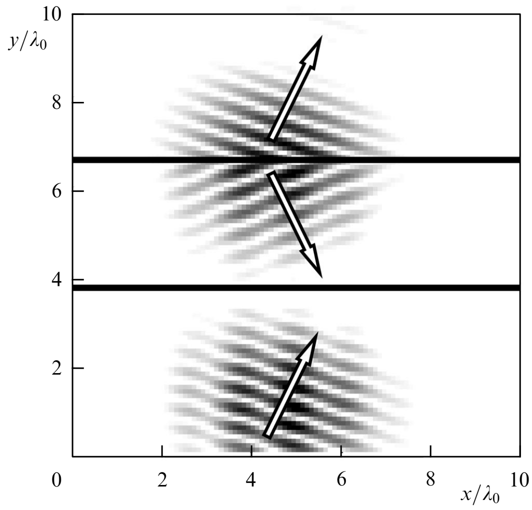

Figure 2. Real part of the acoustic pressure field $p(\mathbf{r}, t)$ calculated at a fixed instant of time during the incidence of pulses, representing a superposition of nine plane monochromatic waves, on a negative-material plate. The plate boundaries are indicated by dark horizontal straight lines. The arrows show the propagation directions of pulses in the plate and environment.

Such a consideration brings up a number of questions. First, a pulse leaving the plate appears before the moment when the incident pulse touches the plate, i.e., the causality principle is violated. Second, the mechanism of the appearance of additional energy on one side of the plate and its absorption on the other side is not quite clear. Third, a pulse propagates in the plate mirror-symmetrically to the traveling direction of a pulse in the environment, i.e., not only the phase but also the group velocities (if we relate the latter to the envelope maximum velocity) are negative. On the other hand, it was pointed out [3] that the phase and group velocities in the negative medium are antiparallel.

The possible answer to the first question is that a periodic time-infinite process is considered and therefore there exist an infinite number of pulses that have propagated through the plate earlier. Then, the observed pulse 'leaving' the plate is the consequence of their propagation rather than the precursor of the pulse incident on the plate. The creation of the pulse is caused by the energy of propagated pulses stored in the plate.

Therefore, because the medium possesses the internal stored energy, this energy storage can decrease during the pulse propagation in it. In this sense, the pulse in a negative medium can have the negative energy (with respect to the environment). Taking this fact into account, the energy conservation law on both boundaries of the plate remains valid: as a pair perturbation is produced on the far side (from a radiation source) of the plate, a pulse with the positive energy propagates in the environment, while in the plate, i.e., in the negative medium, a pulse with the negative energy propagates. These pulses merge on the front side of the plate to produce the zero total energy.

The negativity of both phase and group velocities is due to the fact that simulations were performed assuming that the medium was nondispersing. Negative metamaterials realized in practice, which often contain resonance elements, are strongly dispersing. To understand whether a nondispersing negative medium can exist in principle, we will analyze the propagation of a single pulse (packet) through it, i.e., consider the problem in a broad frequency range. The consideration should be based on the system of equations (1). Then, the field in the medium in the one-dimensional case is described by the Lippmann–Schwinger type equation

$$\begin{pmatrix} p(x,t) \\ v(x,t) \end{pmatrix} = \begin{pmatrix} p_0(x,t) \\ v_0(x,t) \end{pmatrix} - \frac{1}{2}\iint \mathrm{d}x'\,\mathrm{d}t'\,\delta\left(t - t' - \frac{|x-x'|}{c}\right)$$
$$\times \begin{pmatrix} \sqrt{\dfrac{\rho_0}{\eta_0}} & \operatorname{sgn}(x-x') \\ \operatorname{sgn}(x-x') & \sqrt{\dfrac{\eta_0}{\rho_0}} \end{pmatrix} \begin{pmatrix} \eta'(x') & 0 \\ 0 & \rho'(x') \end{pmatrix}$$
$$\times \frac{\partial}{\partial t'} \begin{pmatrix} p(x',t') \\ v(x',t') \end{pmatrix}, \qquad (3)$$

where δ is the Dirac delta function. (The derivation of this equation will be presented in detail elsewhere.) Equation (3) allows one to study the propagation of a single Gaussian packet through a plate made of a negative material.

The results of such a simulation are presented in Fig. 3.The packet width is 1.5 times larger than the plate thickness which is indicated by double vertical straight lines. The coordinate x is plotted on the abscissa, and the quantity $c_0 t$ is plotted along the ordinate. To obtain the field distribution at a certain instant of time, it is necessary to draw a horizontal straight line (section) across the figure. A packet incident on the plate in the positive direction of the x-axis is located in region I. Packets propagating in the plate and environment behind the plate are located in regions II and III, respectively. One of the possible sections, shown by the dashed straight line, corresponds to the instant of time when the center of the primary packet resides at a distance on the order of the plate thickness from the plate. In this case, the field perturbation begins to appear on the opposite side of the plate. Thus, the packet transmitted through the plate appears earlier than the primary incident packet reaches the plate and, therefore, the causality principle is violated in such a medium. It seems that this means that nondispersing negative media cannot exist. In the presence of dispersion in a medium (for example, if a

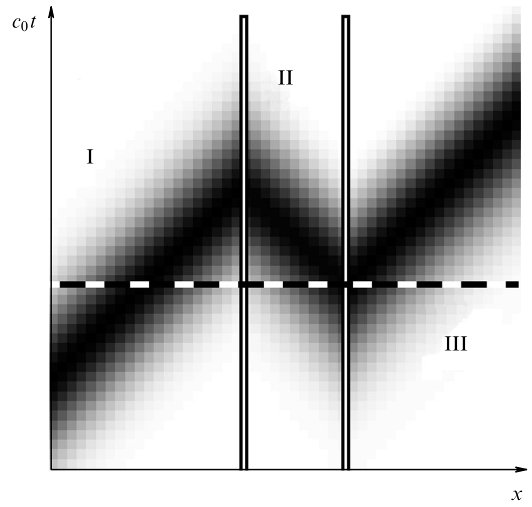

Figure 3. Real part of the acoustic pressure field $p(x, t)$ calculated during the normal incidence of a Gaussian pulse on a negative-material plate. The thick vertical straight lines indicate the plate boundary coordinates. The dashed horizontal straight line corresponds to the instant of time at which the packet center is located at a distance from the plate equal to its thickness, and the field perturbation appears on the far side of the plate.

negative medium is constructed of resonance elements), scalar quantities $\eta'(x)$ and $\rho'(x)$ in equation (3) should be replaced by operators in the form of the time convolution of response functions of resonators. The simulation of this case showed that a precursor packet does not appear, i.e., the causality principle is not violated. Simultaneously, negative refraction is observed in the steady-state regime, which is not accompanied by considerable absorption in a broad frequency band.

3. Angle between the phase and group wave velocities in crystals

It is known that birefringent crystalline media with specifically combined optical and acoustic characteristics are widely used in modern optics, acoustics, acoustooptics, and acoustoelectronics [9–11]. For example, quartz (α-SiO_2), lithium niobate ($LiNbO_3$), calcite ($CaCO_3$), paratellurite (TeO_2) crystals and some others are extensively applied in optical, acoustooptic, and acoustoelectronic devices [9–12]. However, recently crystal materials with a large anisotropy of acoustic and optical properties have found applications in optics, acoustooptics, and acoustics. Such materials include mercury (Hg)- and tellurium (Te)-based single crystals having extremely large birefringence and a strong dependence of the phase velocity of sound on the propagation direction [12].

4. Optical birefringent media

The birefringence Δn of crystalline materials is determined by the difference $\Delta n = n_e - n_o$ of the refractive indices for extraordinarily (n_e) and ordinarily (n_o) polarized light [9, 10]. This difference in some materials can be rather large. For example, the relative birefringence (the anisotropy coefficient) $\delta = \Delta n/n_o$ in tellurium crystals reaches $\delta = 0.3$, and in calomel (Hg_2Cl_2) $\delta = 0.35$. For comparison, birefringence in quartz is two orders of magnitude lower: $\delta = 0.006$ [12, 13].

It is known from optics and electrodynamics that extraordinary waves in materials with large birefringence propagate with angles ψ between the phase and group velocity vectors exceeding 10° [9, 10]. The 'walk-off' angle ψ for the extraordinary optical wave is found from the analysis of the surface of wave vectors in a crystal. The wave surface in a uniaxial optical material represents the ellipsoid of revolution. The value of the wave vector k_e of light in a crystal depends on the light propagation direction with respect to the optical axis Z and changes in a positive crystal within the limits $2\pi n_o/\lambda \leqslant k_e \leqslant 2\pi n_e/\lambda$, where λ is the light wavelength [9, 10]. It is known that the group velocity direction of an electromagnetic wave coincides with the direction of the normal to the wave-vector surface erected at a point in which the wave vector $\mathbf{k}_e$ touches the normal surface. It can be shown that the maximum walk-off angle in a uniaxial crystal is described by the expression [12]

$$\psi_{max} = \arctan \frac{\delta(1 + 0.5\delta)}{1 + \delta} . \qquad (4)$$

Calculations by means of formula (4) show that the angle between the wave phase velocity vector and the Umov–Poynting vector in a negative calcite crystal with the birefringent coefficient $\delta = -0.1$, widely used in polarization devices, is $\psi_{max} = -6°$. The maximum optical walk-off angles in paratellurite and quartz crystals with $\delta = 0.07$ and 0.006 do not exceed $\psi_{max} = 4°$ and $\psi_{max} = 0.4°$, respectively. On the other hand, the maximum walk-off angle in a tellurium crystal with $\delta = 0.3$ is $\psi_{max} = 15°$, while this angle in a mercury bromide (Hg_2Br_2) crystal with $\delta = 0.36$ already reaches a considerable value of $\psi_{max} = 19°$ [12]. Finally, the maximum angle between the Umov–Poynting vector and the wave vector of light in one of the base planes of a biaxial antimony sulfoiodide (SbSI) crystal with the record-high birefringence $\delta = 0.6$ [13] is $\psi_{max} \approx 25°$.

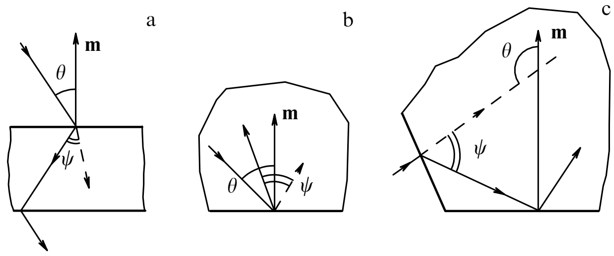

Figure 4. Cases of the unusual propagation and refraction of light waves in birefringent crystals. The direction of the phase velocity of light is shown by dashed straight lines and arrows, and the energy flux direction is indicated by solid straight lines and arrows: (a) the propagation of a light wave through a plane-parallel plate; (b) anomalous internal reflection of light from a crystal–vacuum interface, and (c) the incidence of light on an interface at an angle θ exceeding 90°.

The anisotropy of physical properties resulting in large angles between the phase and group velocities of optical waves can lead to unusual cases of propagation and reflection of these waves from the crystal–vacuum interface. Some of these cases of wave propagation are illustrated in Fig. 4. Figure 4a demonstrates the oblique incidence at an angle of θ and propagation of a light beam through a birefringent crystal plane-parallel plate. The angle of incidence is traditionally measured between the wave vector and the normal $\mathbf{m}$ to the interface. The directions of the electromagnetic energy flux and the group velocity vector in the beam are shown by the arrows and solid straight lines, while the direction of the phase velocity of light is indicated by the dashed arrow and the straight line. One can see from the figure that the energy flux refracted in the plate is directed anomalously, i.e., just as this occurs in metamaterials. The refraction angle for the energy flux proves to be negative, although the wave vector of light is oriented with respect to the normal strictly in accordance with Snell's law. Therein lies the difference between the classical case of light propagation in a crystal and the propagation of light in a metamaterial. Obviously, the anomalous refraction of the optical beam in Fig. 4a is caused by a large optical walk-off angle ψ.

Figure 4b demonstrates the unusual reflection of a light beam from the interface during the propagation of a light wave through a birefringent crystal. One can see from this figure that, because of the large optical anisotropy of the material, the energy fluxes of the incident and reflected optical beams are located on the one side of the normal to the interface. Finally, Fig. 4c illustrates the propagation of light in the crystal and its incidence at an angle of θ to the crystal–vacuum interface exceeding 90°. The wave vector of light at such an anomalously large angle of incidence is found directed not to the interface side but from it, while the energy flux of the optical wave hits the interface. Obviously, these unusual effects are caused by the considerable optical anisotropy of the crystal.

5. Acoustic anisotropic media

Acoustic media are known to possess even the more pronounced anisotropy of physical properties compared to that in optical media. An acoustic crystal with the large anisotropy of elastic properties is characterized by a strong dependence of the phase velocity v of ultrasound on its propagation direction [11–16]. For example, a slow shear acoustic wave in a calomel (Hg_2Cl_2) crystal propagates along the [110] axis with the anomalously slow velocity $v = 347$ m s^{-1}, whereas the same acoustic mode propagating along the [100] and [010] axes has the velocity $v = 1305$ m s^{-1} [13–15]. Thus, the ratio of the maximal and minimal phase velocities of sound in calomel for this acoustic mode is $r = 3.76$. In mercury bromide (Hg_2Br_2) and iodide (Hg_2I_2) crystals, the ratio of acoustic velocities reaches $r = 4.39$ and 4.89, respectively. Finally, the acoustic anisotropy coefficient in a paratellurite (TeO_2) crystal is $r = 4.95$. The large spatial dispersion of acoustic velocities leads to extremely large acoustic walk-off angles ψ, i.e., angles between the wave vector and the Umov–Poynting vector. Thus, for example, the acoustic walk-off angle in a calomel crystal is equal to $\psi = 70°$. Similarly, the acoustic walk-off angle in a mercury bromide crystal reaches $\psi = 72°$, while the wave vectors of the phase and group velocities in Hg_2I_2 and TeO_2 crystals are separated by a very large angle $\psi = 74°$. It should be noted that rather large acoustic walk-off angles are also typical for many other acoustic materials. For example, the walk-off angles in a double lead molybdate (Pb_2MoO_5) crystal and a tellurium crystal are $\psi = 69°$ and 56°, respectively [17].

The unusually large angles between the phase and group velocities of acoustic waves lead to many unusual wave phenomena observed at crystal–vacuum or crystal–isotropic medium interfaces. One such unusual phenomenon is the nearly backward reflection of the acoustic energy in a paratellurite crystal during the glancing incidence of a wave on the free crystal–vacuum interface [15, 16, 18, 19].

The case of a grazing incidence of the elastic energy on a free face of a paratellurite crystal is illustrated in Fig. 5. A piezoelectric transducer excites an acoustic wave in the crystal with the phase velocity and wave vector directed horizontally, i.e., at an angle of incidence $\theta = 90°$ with respect to the normal **m** to the upper boundary of the crystal. One can see from the figure that the group velocity of the initial wave is directed towards the upper face of the crystal, and therefore the acoustic energy is incident on the interface obliquely, as shown in Fig. 5a. The group velocity vector of the acoustic wave reflected from the upper face of the crystal is, in fact, antiparallel to the incident wave energy flux. Calculations predict that the spatial angle γ between the energy fluxes of the incident and reflected waves does not exceed 6°.

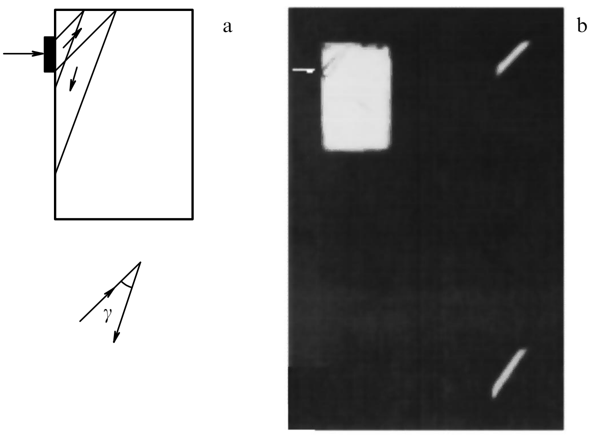

Figure 5. Nearly backward reflection of the acoustic energy from a crystal–vacuum interface during the glancing incidence of an acoustic wave front on the interface: (a) the general view of the crystal and the propagation directions of energy fluxes shown by the arrows, and (b) the visualization of acoustic fields in a paratellurite crystal by the acoustooptic method.

The wave vector of the reflected acoustic wave is spatially oriented in strict accord with the known condition for the equality between tangential projections of the wave vectors of incident and reflected waves onto the interface [14, 15]. The unusual backward propagation of the reflected acoustic energy is caused by the large acoustic walk-off angle in paratellurite. It turns out that, in the case of unusual reflection, almost all the energy of the incident acoustic wave can be converted without losses to the energy of the backward reflected wave.

6. Observation of the unusual reflection of acoustic waves

The unusual reflection of acoustic waves was experimentally confirmed by the acoustooptic method via visualization of acoustic fields and illumination of a TeO_2 crystal by a broad collimated 633-nm beam from an He–Ne laser [18, 19]. Longitudinal acoustic waves were excited by a lithium niobate piezoelectric transducer at the ultrasonic frequency $f = 150$ MHz. The linear dimensions of the transducer, 0.3×0.5 cm, exceeded the ultrasonic wavelength in the crystal by a few orders of magnitude. Therefore, the acoustic waves were treated in the experiments as plane waves.

Figure 5b displays the general view of the diffraction pattern observed at the crystal output. The presence of a visualized acoustic column in the lower right corner of the photograph, which was oriented parallel to the reflected acoustic column shown in Fig. 5a, proves that it was the backward reflection of acoustic waves that was detected in experiments [18, 19]. The angle γ between the group velocity vectors of the incident and reflected acoustic waves was measured to be 9°, with the calculated angle being 6°.

Our analysis has evidenced that the unusual cases of propagation, reflection, and refraction of light waves shown in Fig. 4 can also be easily realized in acoustic crystals. Thus, unusual wave phenomena with anomalously directed waves can be observed in both optics and acoustics. Although the physical nature of these phenomena and effects differs from that in metamaterials, they are manifested similarly to those in double negative media. Notice that the unusual propagation and reflection of waves occur not only in anisotropic media known in optics and acoustics. For example, the propagation of electromagnetic waves in thin magnetic films is also characterized by large angles between the phase velocity vector and the Umov–Poynting vector [20].

7. Orientation of the phase and group velocity vectors in anisotropic media and metamaterials

Generalizing results of studies into the propagation of acoustic waves in optical and acoustic media [12, 15–20], we can propose a unified view of wave processes proceeding in crystals, anisotropic media, and artificial periodic structures in electrodynamics, optics, and acoustics. The conditional direction of the phase velocity of a plane bulk wave propagating in an anisotropic medium is indicated in Fig. 6 along the horizontal direction (the x-axis). According to the conclusions presented in Section 4, angles between the wave

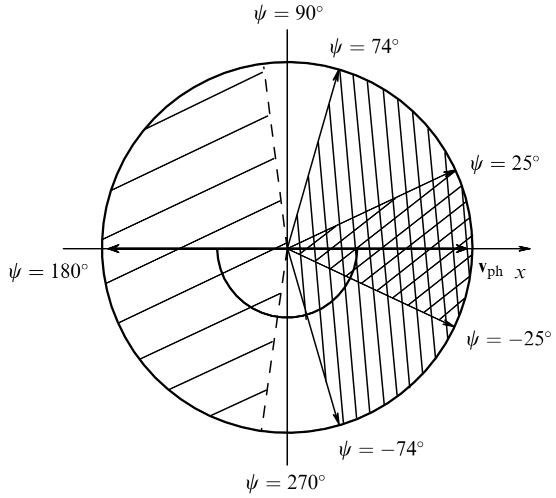

Figure 6. Orientation of the group-velocity vector with respect to the phase velocity vector of optical and acoustic waves in crystals and metamaterials.

vector of the extraordinary light wave and the Umov–Poynting vector in birefringent crystals can lie within the limits $-25° < \psi < 25°$, as shown in Fig. 6. In acoustic anisotropic media, angles between the phase and group velocities of the waves lie in the range $-74° < \psi < 74°$. Thus, almost the entire right half of the diagram in Fig. 6 describes wave processes typical of optics and acoustics.

The propagation of waves in metamaterials and double negative acoustic media with the Umov–Poynting vector antiparallel to the wave vector corresponds in Fig. 6 to the horizontal direction oriented at an angle of $\psi = 180°$ relative to the initial wave vector. In this connection, it is interesting to determine the waves corresponding to the energy walk-off angles lying in the ranges $90° < \psi < 180°$ and $180° < \psi < 270°$ in the diagram. Our analysis suggests that the left part of the diagram describes waves propagating in artificial media, i.e., metamaterials. However, these media should have the anisotropy of physical properties providing the propagation of waves not only with the antiparallel phase and group velocity vectors but also at angles different from $\psi = 180°$. Obviously, such artificial media should also possess a strong spatial anisotropy of physical properties.

By analyzing the data presented in Fig. 6, we should consider separately the cases of the group velocity directed at angles of $\psi = 90°$ and $270°$ to the phase velocity vector. It is well known from optics and acoustics that the group velocity of a wave in a crystal exceeds in absolute value the phase velocity, these velocities being related by the expression $v_{\mathrm{ph}} = v_{\mathrm{g}} \cos\psi$, where ψ is the angle between the phase and group velocities [9, 10, 14]. It follows from this relation that for walk-off angles $\psi = 90°$ and $270°$ and the finite group velocity of the wave, its phase velocity vanishes. In other words, when the phase and group velocities are mutually orthogonal, the concept of a 'wave' becomes completely meaningless. Similarly, when the phase velocity is finite, it follows from the last relation that the energy transfer rate becomes infinite, which also contradicts the physical sense. Thus, we can assume that wave processes with the orthogonal phase and group velocities of volume waves are absent in optical and acoustic media.

8. Conclusion

The description of wave acoustic processes directly based on hydrodynamic equations and an analogue of the Lippmann–Schwinger equation is correct both for classical (positive) and negative media. The propagation of a wave packet in a plate made of a negative material, assuming the absence of dispersion, gives rise to a precursor packet behind the plate, which contradicts the causality principle. This does not occur when the response of the metamaterial is resonant in character.

The strong anisotropy of the optical and elastic properties of crystals leads to the unusual propagation and 'negative' reflection of waves in these materials. The reflection of elastic waves from a free surface separating a crystal and a vacuum can be accompanied by the propagation of the reflected-wave energy almost antiparallel to the energy flux of the incident wave.

Acknowledgments

This work was supported by NSh 4590.2010.2, MK 2041.2011.5, and MK-1643.2011.8 grants of the President, Russian Federation, and the Russian Foundation for Basic Research (grants 10-02-00636a, 10-05-00229a, and 10-07-00683a). Studies related to this work were also supported by a CRDF RUP1-1663-MO-06 grant, and 2010-220-01-077 grant of the Russian Federation Government (contract 11.G34.31.0005).

References

1. Veselago V G *Usp. Fiz. Nauk* **92** 517 (1967) [*Sov. Phys. Usp.* **10** 509 (1968)]
2. Smith D R et al. *Phys. Rev. Lett.* **84** 4184 (2000)
3. Burov V A, Dmitriev K V, Sergeev S N *Akust. Zh.* **55** 292 (2009) [*Acoust. Phys.* **55** 298 (2009)]
4. Chan C T, Li J, Fung K H *J. Zhejiang Univ. Science A* **7** 24 (2006)
5. Li J, Chan C T *Phys. Rev. E* **70** 055602(R) (2004)
6. Wu Y, Lai Y, Zhang Z-Q *Phys. Rev. B* **76** 205313 (2007)
7. Smith D R, Kroll N *Phys. Rev. Lett.* **85** 2933 (2000)
8. Bliokh K Yu, Bliokh Yu P *Usp. Fiz. Nauk* **174** 439 (2004) [*Phys. Usp.* **47** 393 (2004)]
9. Born M, Wolf E *Principles of Optics* (Oxford: Pergamon Press, 1969) [Translated into Russian (Moscow: Nauka, 1970)]
10. Yariv A, Yeh P *Optical Waves in Crystals* (New York: Wiley, 1984) [Translated into Russian (Moscow: Mir, 1987)]
11. Balakshii V I, Parygin V N, Chirkov L E *Fizicheskie Osnovy Akustiki* (Physical Foundations of Acoustics) (Moscow: Radio i Svyaz', 1985)
12. Voloshinov V B, Mosquera J C *Opt. Spektrosk.* **101** 675 (2006) [*Opt. Spectrosc.* **101** 635 (2006)]
13. Blistanov A A et al. *Akusticheskie Kristally* (Acoustic Crystals) (Ed. M P Shaskol'skaya) (Moscow: Nauka, 1982)
14. Auld B A *Acoustic Fields and Waves in Solids* (Malabar, Fla.: R.E. Krieger, 1990)
15. Voloshinov V B, Polikarpova N V, Declercq N F *J. Acoust. Soc. Am.* **125** 772 (2009)
16. Voloshinov V B, Polikarpova N V, Mozhaev V G *Akust. Zh.* **52** 297 (2006) [*Acoust. Phys.* **52** 245 (2006)]
17. Voloshinov V B et al. *J. Opt. A* **10** 095002 (2008)
18. Voloshinov V B, Polikarpova N V *Appl. Opt.* **48** C55 (2009)
19. Voloshinov V B, Makarov O Yu, Polikarpova N V *Pis'ma Zh. Tekh. Fiz.* **31** (8) 79 (2005) [*Tech. Phys. Lett.* **31** 352 (2005)]
20. Lock E H *Usp. Fiz. Nauk* **178** 397 (2008) [*Phys. Usp.* **51** 375 (2008)]

PACS numbers: 03.65.Xp, **42.25.**–p, **78.67.**–n
DOI: 10.3367/UFNe.0181.201111j.1212

Resonant tunneling of ultrashort electromagnetic pulses in gradient metamaterials: paradoxes and prospects

A B Shvartsburg, N S Erokhin

1. Introduction. Tunneling of a monochromatic wave through a gradient photonic barrier (exactly solvable model)

This report is devoted to new effects of wave-pulse tunneling through inhomogeneous media. The concept of tunneling often refers to quantum effects of particle penetration through potential barriers with the heights exceeding the energy of the particles themselves. It is this problem that was first solved by G A Gamow in 1928 [1] when E Rutherford asked him to explain the paradox of the alpha decay of atomic nuclei, in which the energy of an alpha particle leaving a nucleus proved to be lower than the height of a potential barrier surrounding the nucleus. By using the formal analogy between the classical wave equation and the Schrödinger equation, Gamow managed to show that a partial penetration of de Broglie waves describing an alpha particle through the barrier corresponds to the frustrated total internal reflection effect known in optics. Such a penetration mechanism, which is impossible in classical mechanics, was called 'tunneling'. By connecting this analogy with the uncertainty in the relation between the momentum and coordinate of a quantum particle, Gamow calculated the exponentially small but finite probability of particle tunneling through the barrier. This was probably the first application of quantum mechanics in nuclear physics, and became for many years an etalon for describing the tunneling of quantum objects in electronics and solid state physics.

Tunneling effects attracted new interest with the development of metamaterials and, especially, in connection with advances in nanotechnologies in the manufacturing of so-called gradient media with electromagnetic or mechanical parameters continuously distributed inside a medium according to a specified law managed by the manufacturing technology. Studies were devoted not to traditional quantum problems, but to classical problems of the propagation of electromagnetic waves through gradient finite-thickness dielectric layers. In nanophotonics, such layers are called 'gradient photonic barriers', while in the radiophysics of superhigh-frequency electromagnetic waves, they are called gradient wave barriers. It is these structures that are now attracting attention in the development of a new generation of photonic crystals, guiding wave systems, and miniature radioelectronic devices.

A B Shvartsburg Joint Institute for High Temperatures, Russian Academy of Sciences, Moscow, Russian Federation, and the Space Research Institute, Russian Academy of Sciences, Moscow, Russian Federation
E-mail: alex-s-49@yandex.ru
N S Erokhin Space Research Institute, Russian Academy of Sciences, Moscow, Russian Federation. E-mail: nerokhin@mx.iki.rssi.ru

Uspekhi Fizicheskikh Nauk **181** (11) 1212–1217 (2011)
DOI: 10.3367/UFNr.0181.201111j.1212
Translated by M N Sapozhnikov; edited by A Radzig

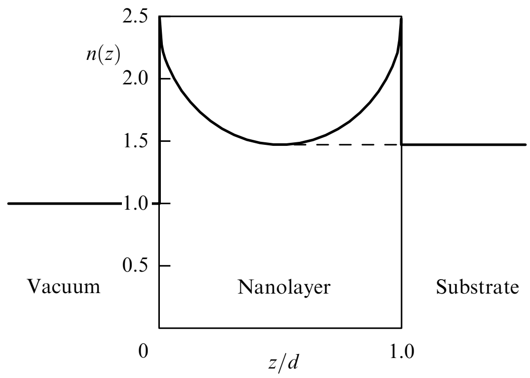

Figure 1. Normalized permittivity profile (1) inside a gradient photonic barrier providing the tunneling of electromagnetic waves through a barrier with width d; z/d is the dimensionless coordinate across the barrier.

As shown in review [2], the physical foundations of tunneling electromagnetic waves through gradient media are determined by geometrical or nonlocal dispersion. This mechanism is not related to the material dispersion of the barrier material and depends on the gradient and curvature of the spatial profile of the refractive index $n(z)$. Artificial dispersion effects are considered in this paper for transparent barriers obtained by the deposition of a dielectric onto a homogeneous nonabsorbing substrate with the refractive index n. The exact analytical solutions to Maxwell's equations for a number of such gradient photonic barriers demonstrate the peculiarity of wave tunneling processes in gradient nanooptics, which consists, in particular, of the following [3]:

(1) The reflection and transmission spectra of gradient media are determined not only by the jump of the refractive index $n(z)$ on the medium boundary, but also by the discontinuities of the gradient and curvature of the refractive index profile $n(z)$. The expressions for reflection and transmission spectra were obtained for a number of $n(z)$ profiles, the classical Fresnel formulae being merely a particular case of these expressions. Thus, the normalized $n(z)$ profile (Fig. 1) containing two arbitrary spatial scales L_1 and L_2, namely

$$n(z) = n_0 U(z)\,, \qquad U(z) = \left(1 + \frac{z}{L_1} - \frac{z^2}{L_2^2}\right)^{-1}, \tag{1}$$

is characterized by the cutoff frequency Ω [3] depending on the barrier thickness d, the refractive index n_0 of the barrier material, and geometrical parameters of profile (1):

$$\Omega = \frac{2cy\sqrt{1+y^2}}{n_0 d}\,, \qquad y = \frac{L_2}{2L_1}\,. \tag{2}$$

The transmittance of a gradient wave barrier (1) with cutoff frequency (2) is determined by the waveguide type dispersion: waves with frequencies $\omega > \Omega$ propagate through the barrier in the traveling-wave regime, while waves with frequencies $\omega < \Omega$ propagate in the tunneling regime. The tunneling spectra of barrier (1) can be conveniently considered using the dimensionless frequency $u = \Omega/\omega$. In this case, the regime of $\omega > \Omega$ ($\omega < \Omega$) corresponds to the condition $u < 1$ ($u > 1$). The complex transmission coefficient $T = |T| \exp(\mathrm{i}\phi_{\mathrm{t}})$ of barrier (1) in the traveling-wave regime is described by the expressions [3]

$$|T|^2 = \frac{4nn_{\rm e}^2(1+t^2)}{|\Gamma|^2}\,, \tag{3}$$

$$|\Gamma|^2 = \left[t\left(n - \frac{\gamma^2}{4} + n_{\rm e}^2\right) + \gamma n_{\rm e}\right]^2 + (n+1)^2\left(n_{\rm e} - \frac{\gamma t}{2}\right)^2, \tag{4}$$

$$\cos\phi_{\rm t} = \frac{(n+1)(n_{\rm e} - \gamma t/2)}{|\Gamma|}\,, \qquad \sin\phi_{\rm t} = \frac{t(n - \gamma^2/4 + n_{\rm e}^2) + \gamma n_{\rm e}}{|\Gamma|}\,, \tag{5}$$

$$t = \tan\left(l\sqrt{\frac{1}{u^2} - 1}\right), \qquad n_{\rm e}^2 = n_0^2(1-u^2)\,, \tag{6}$$

$$\gamma = \frac{2n_0uy}{\sqrt{1+y^2}}\,, \qquad l = \ln\frac{y_+}{y_-}\,, \qquad y_\pm = \sqrt{1+y^2} \pm y\,. \tag{7}$$

The complex transmission coefficient $T = |T|\exp(\mathrm{i}\phi_{\rm t})$ of the barrier in the tunneling regime is described by other expressions

$$|T|^2 = \frac{4nn_{\rm e}^2(1-t^2)}{|\aleph|^2}\,, \tag{8}$$

$$|\aleph|^2 = \left[t\left(n - \frac{\gamma^2}{4} - n_{\rm e}^2\right) + \gamma n_{\rm e}\right]^2 + (n+1)^2\left(n_{\rm e} - \frac{\gamma t}{2}\right)^2, \tag{9}$$

$$\cos\phi_{\rm t} = -\frac{(n+1)(n_{\rm e} - \gamma t/2)}{|\aleph|}\,, \qquad \sin\phi_{\rm t} = -\frac{t(n - \gamma^2/4 - n_{\rm e}^2) + \gamma n_{\rm e}}{|\aleph|}\,, \tag{10}$$

$$n_{\rm e}^2 = n_0^2(u^2 - 1)\,, \qquad t = \tanh\left(l\sqrt{1 - \frac{1}{u^2}}\right). \tag{11}$$

Parameters γ and l entering formulas (8)–(11) are defined in Eqn (7).

(2) Analysis of expressions (3)–(11) for the complex transmission coefficient $T = |T|\exp(\mathrm{i}\phi_{\rm t})$ shows that, on passing from the traveling-wave regime to the tunneling regime ($u = 1$), the modulus of the coefficient, $|T|$, changes continuously (Fig. 2a), while the phase $\phi_{\rm t}$ experiences a jump by π (Fig. 2b).

(3) The permittivity, unlike that in conventional electromagnetic-wave tunneling effects in media with free carriers, preserves the positive real value at all points inside a nanofilm ($0 < z < d$), in particular, on the descending branch of the $\varepsilon(z)$ profile ($0 \leqslant z \leqslant d/2$), where the condition $\mathrm{grad}\,\varepsilon < 0$ is fulfilled for $\varepsilon > 0$. The interference of the forward and backward waves in the gradient barrier can lead not to the known effects of strong reflection of the incident wave and exponential decay of the tunneling field in a homogeneous rectangular barrier, but to an almost reflectionless (resonance) tunneling regime in some spectral interval. The transmission coefficient squared $|T|^2$ in such a state can reach high values of $|T|^2 = 0.9-0.95$, and even $|T|^2 = 1$.

2. Dynamics of an ultrashort pulse during resonance tunneling

The properties of monochromatic fields pointed out in Refs [2, 3] are used here to analyze the tunneling of ultrashort broadband one- or few-cycle femtosecond pulses and video pulses through a gradient photonic barrier. The tunneling of such pulses is considered below without any new physical hypothesis and mathematical approximations based on Maxwell's equations for the exactly solvable model of this barrier.

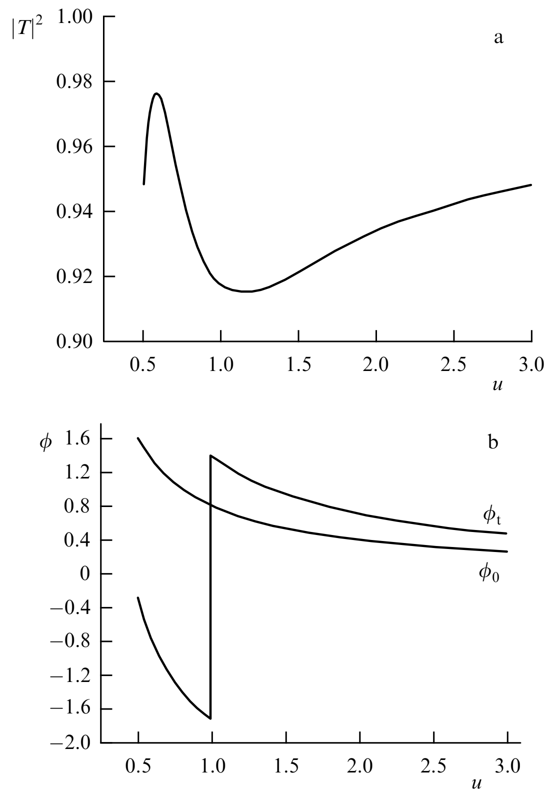

Figure 2. Tunneling spectra for the gradient barrier depicted in Fig. 1, with parameters $n_0 = 2.3$, $n_{\min} = 1.47$, and $d = 100$ nm. (a) Energy transmission coefficient $|T|^2$. (b) Phase shift $\phi_{\rm t}$ of the transmitted wave; ϕ_0 is the wave phase incursion in air, and $u = \Omega/\omega$ is the normalized frequency.

Consider a barrier formed by a transparent dielectric nanolayer with width d and continuous profile (1) plotted in Fig. 1 (curve *1*). The nanolayer is deposited onto a thick homogeneous substrate with the refractive index n. The refractive index achieves maximum values of $n = n_0$ on the layer boundaries $z = 0$ and $z = d$, and a minimum value of $n = n_{\min}$ at $z = 0.5d$. The cutoff frequency Ω of such a gradient barrier is determined by expression (4). The amplitude–phase transmission spectra in the vicinity of the normalized cutoff frequency $u = \Omega/\omega = 1$, plotted by expressions (3)–(11) for the complex transmission coefficient $T = |T|\exp(\mathrm{i}\phi_{\rm t})$ of the barrier, are displayed in Fig. 2.

One can see from Fig. 2 that the energy transmission coefficient $|T|^2$ for $u = 1$ is continuous, whereas the phase spectrum of the transmitted wave for $u = 1$ exhibits a jump by π [4]: the values of $\phi_{\rm t}(\omega)$ in the tunneling regime ($\omega \leqslant \Omega$, $u \geqslant 1$) are positive, and they are negative in the traveling-wave regime ($\omega \geqslant \Omega$, $u \leqslant 1$). The phase shift $\phi_{\rm t}$ in the tunneling regime can exceed in some frequency interval the phase shift ϕ_0 of a wave with the same frequency ω propagating through the same distance d in free space ($\phi_0 = \omega d/c$). These superluminal ($\phi_{\rm t} > \phi_0$) and subluminal ($\phi_{\rm t} < \phi_0$) phase effects are exemplified in Fig. 2b.

Consider the tunneling of a femtosecond pulse with duration t_0, carrier frequency ω_0, amplitude E_0, and envelope

$$E(t) = E_0 \sin\frac{\pi t}{t_0}\cos(\omega_0 t)\,, \tag{12}$$

incident normally on a gradient barrier with the transmission spectra displayed in Fig. 2. The spectrum of pulse (12) contains harmonics belonging both to the traveling-wave and tunneling regions. The phase shifts ϕ_t in these regions have opposite signs, and the frequency dispersion of phase spectra is considerable in both regions (Fig. 2b). The contributions of harmonics with $\phi_t < 0$ and $\phi_t > 0$ to the envelope of the tunneling pulse prove to be dependent on the detuning of the carrier frequency ω_0 from the cutoff frequency Ω. The pulse envelope after tunneling through the gradient barrier is constructed by using the inverse Fourier transform of the product $F(\omega)\,T(\omega)$, where $F(\omega)$ is the Fourier transform of an initial pulse (12), and $T(\omega)$ is the complex transmission coefficient. To take into account contributions from both subluminal and superluminal phase shifts to the formation of the tunneling envelope $E_1(t)$, the inverse Fourier transform is performed in the ω-frequency range from 0 to ∞.

The tunneling pulse dynamics can be conveniently considered in a coordinate system moving together with the leading edge of the pulse in free space at the velocity c. The points of the envelope located behind (ahead) of this leading edge correspond to positive (negative) times, the pulse onset corresponding to the instant $t = 0$. Figure 3 plotted in this coordinate system shows the superluminal displacements of the deformed envelope caused by tunneling frequencies ($u > 1$) in the region $t < 0$ [4]; propagating frequencies ($u < 1$) determine deformation in the subluminal region $t > 0$. The inequality between phase shifts of different harmonics leads to the oscillating broadening of the transmitted pulse and the superluminal shift of its leading edge accompanied by some loss in the pulse energy [$|T|^2 = 0.91$–0.92 (Fig. 2a)]. The normalized envelopes $E_1(t)/E_0$ of transmitted pulses are depicted in Fig. 3. A comparison of these envelopes shows that the distortion of tunneling pulses critically depends on the carrier-frequency detuning $\Delta = (\omega_0 - \Omega)/\Omega$ with respect to the cutoff frequency Ω.

Figure 3a, corresponding to the negative detuning $\Delta = -8.16 \times 10^{-2}$, gives evidence that precursors formed at the leading edge of the tunneling pulse are located in the region $t < 0$, therefore leaving behind the leading edge of the freely propagating pulse ($t = 0$); the amplitude of these precursors, equal to 0.2 at the point $t = 0$, decreases sidewise of the pulse propagation. The modulation of the trailing edge in the region $t > 0$ is provided by propagating frequencies ($u < 1$). In the case of the zero detuning ($\omega_0 = \Omega$ and $\Delta = 0$), the pulse is completely split, producing two peaks with the amplitude 0.7; the precursor amplitude on the pulse leading edge at the point $t = 0$ increases to 0.48. Finally, as the carrier frequency shifts to the traveling region ($\Delta = 4.08 \times 10^{-2} > 0$), the modulation of the fronts of the tunneling pulse and splitting of the maximum become less pronounced (Fig. 3d).

Notice that these deformations appear when pulse (12) propagates through a thin gradient barrier with width $d = 100$ nm much smaller than the wavelength λ (800 nm) corresponding to the carrier frequency ω_0. This effect is typical precisely for a gradient barrier: one can see from Fig. 4 that when pulse (12) with the same carrier frequency ω_0 propagates through a homogeneous barrier, which does not have the cutoff frequency ($\Omega = 0$) and has all the other parameters $(n_0, n_{\min}, n, d)$ coinciding with those for the above-discussed gradient barrier, the tunneling regime and pulse splitting do not appear.

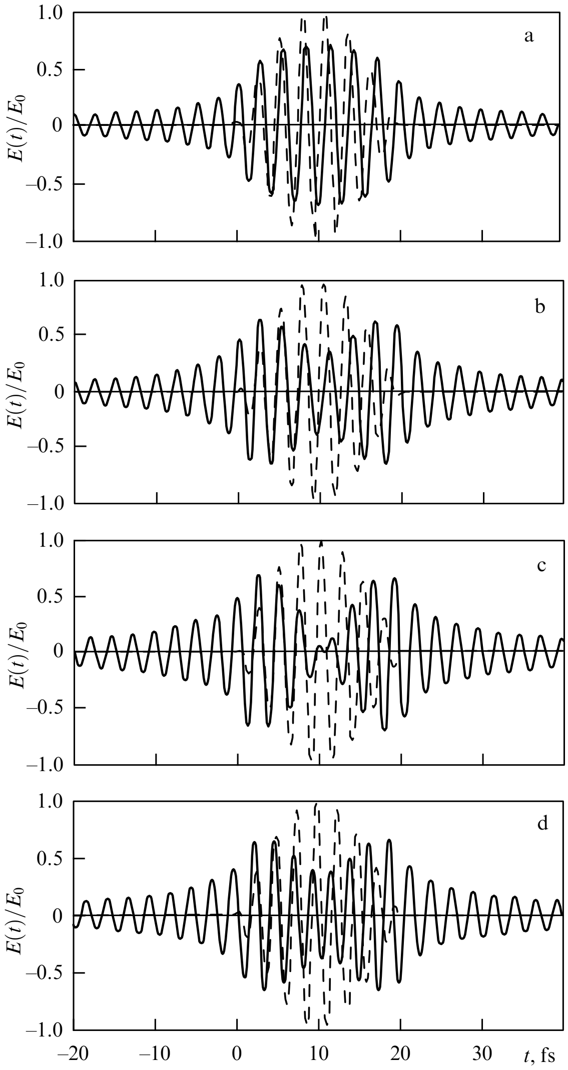

Figure 3. Normalized time envelopes $E(t)/E_0$ of a femtosecond pulse (12) ($t_0 = 20$ fs) propagating in free space (dashed curves), and a pulse tunneling through a gradient barrier (solid curves), $\Omega = 2.45 \times 10^{15}$ rad s^{-1}; carrier frequencies and detunings in Figs 3a–d are $\omega_0 = 2.25 \times 10^{15}$, 2.35×10^{15}, 2.45×10^{15}, and 2.55×10^{15} rad s^{-1}, and $\Delta = -8.16 \times 10^{-2}$, -4.08×10^{-2}, 0, and 4.08×10^{-2}, respectively. Superluminal precursors are formed in the region of $t < 0$.

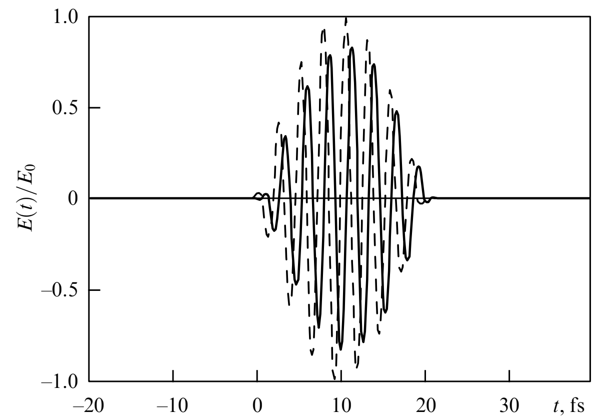

Figure 4. Transmission of pulse (12) with $\omega_0 = 2.45 \times 10^{15}$ rad s^{-1} in the traveling-wave regime through a homogeneous wave barrier ($\Omega = 0$) with parameters n_0, $n_{\min}$, n, and d indicated in the caption to Fig. 2. Unlike the tunneling regime (Fig. 3), no pulse precursors are formed.

It should be noted that during tunneling the 'center of gravity' t_c of the pulse $f(t)$ shifts with respect to the center t_{c0} of a pulse propagating in a vacuum at the speed of light, $\Delta_t = t_{c0} - t_c$, where

$$t_c = \frac{\int_{-\infty}^{\infty} t f(t)\,\mathrm{d}t}{\int_{-\infty}^{\infty} f(t)\,\mathrm{d}t} \, . \tag{13}$$

Calculations using expression (13) reveal that, during tunneling of pulse (12) ($t_0 = 20$ fs), the pulse shift $\Delta_t \approx 0.15-0.2$ fs, i.e., the center of gravity of the pulse after tunneling *lags* behind the center of gravity of a freely propagating pulse ($\Delta_t > 0$).

3. Formation of superluminal precursors during tunneling of a short pulse

At first glance, the modulation of the envelope at the pulse edges resembles the classical Sommerfeld–Brillouin effect — the formation of precursors during the propagation of a pulse in a transparent dispersive medium outside the tunneling region. It is well known that the formation path of these precursors should be long enough ($Z \gg ct_0$), their amplitude should be small compared to the peak amplitude of the pulse, and their velocity does not exceed the speed of light c in a vacuum [5]. However, the results of formation of superluminal precursors [4] during pulse tunneling through a gradient barrier (see Fig. 3) strongly differ from those in the classical picture.

(1) Because of the phase jump producing the fast shift of tunneling harmonics, the considerable deformation of the pulse is developed at distances smaller than the wavelength.

(2) The amplitudes of precursors are not small and can be comparable to the initial pulse peak.

(3) The partial or complete pulse splitting resulting in the formation of precursors is determined by the frequency detuning Δ.

Speaking of the formation of superluminal precursors of the pulse transmitted through a gradient barrier in the tunneling regime, we should point out differences between the basic parameters of the transmitted and initial pulses:

(a) the energy of the transmitted pulse is lower than that of the initial pulse, while its duration is longer compared to the initial pulse. Moreover, the envelope of the transmitted pulse has nothing in common with the initial envelope;

(b) the rate v_g of energy transfer by the tunneling wave inside the barrier, defined as $v_g = P/W$, where P is the Umov–Poynting vector, and W is the energy density, is less than the speed of light c in a vacuum (Fig. 5);

(c) the center of gravity of the transmitted pulse lags behind the center of gravity of the same freely propagating pulse.

The precursor formation rate depends on the number m of field oscillations inside the tunneling pulse with the carrier frequency ω_0 and duration t_0 ($m \approx \omega_0 t_0/(2\pi)$) and the amplitude build-up rate from a periphery to maximum, this rate being related to the parameter m. Under conditions specified in the caption to Fig. 3 ($m = 7-8$), precursors and the splitting of the maximum are well pronounced, while in the case of $t_0 = 100$ fs at the same carrier frequency, m is much greater ($m = 37-38$), the amplitude build-up rate is slower, and a weak modulation appears only in the envelope wings (Fig. 6), while the central peak is not split. To exclude the possible influence of artificial 'end points' of the envelope appearing in model (12), paper [4] reported on the tunneling

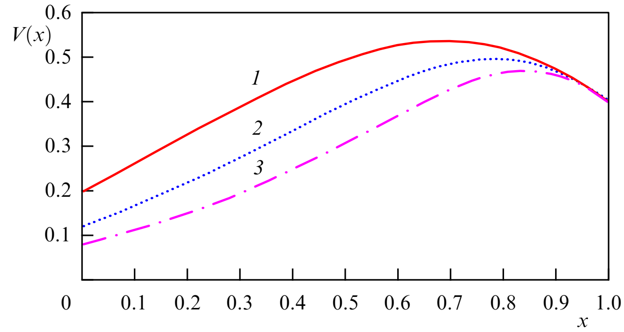

Figure 5. Dispersion of the normalized group velocity $V(x) = v_g/c$ inside the gradient photonic barrier shown in Fig. 1; $x = z/d$ is the dimensionless coordinate. Curves *1*, *2*, and *3* correspond to normalized frequencies $u = 1.0$, 1.5, and 2.0.

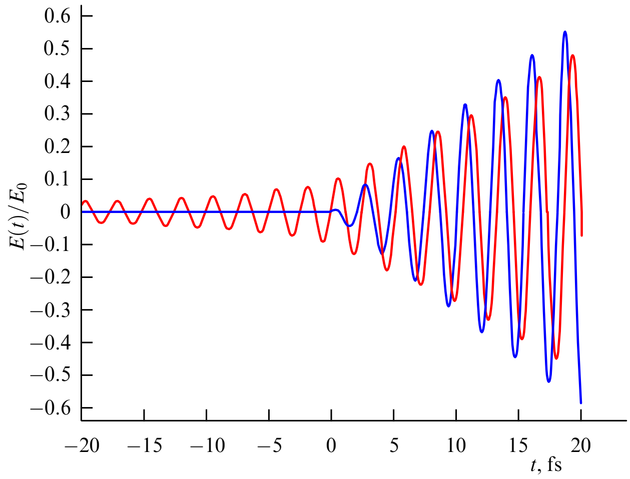

Figure 6. Weak modulation of the envelope ($E/E_0 \leqslant 0.05$) at the periphery of the 'long' pulse (12) ($t_0 = 100$ fs) tunneling through a barrier under conditions of Fig. 3; $\omega_0 = 2.562 \times 10^{15}$ rad s^{-1}.

dynamics of a 'smooth' Gaussian pulse, in which a slow decrease of the envelope in the wings is not related to these points:

$$E(t) = E_0 \exp\left(-\frac{t^2}{t_1^2}\right) \cos(\omega_0 t) \, . \tag{14}$$

The characteristic time t_1 in formula (14) is selected so that t_0, determining the duration of pulse (12), corresponds to the half-width of the Gaussian pulse (14), i.e., $t_1 = 1.2 t_0$.

A comparison of the tunneling of pulses (12) and (14) through the same barrier at the same carrier frequencies ω_0 shows that the envelope experiences splitting in the case of a Gaussian pulse as well, and a superluminal precursor is formed at its leading edge.

Similar effects are also observed during tunneling of ultrashort broadband video pulses containing one or several anharmonic field oscillations and a long decaying 'tail' [6]. An example of such a transformation of a video pulse with the envelope constructed from the Laguerre functions, namely

$$\frac{E(t)}{E_0} = \frac{1}{2}\, x(x-4) \exp\left(-\frac{x}{2}\right), \qquad x = \frac{t}{t_0} \, , \tag{15}$$

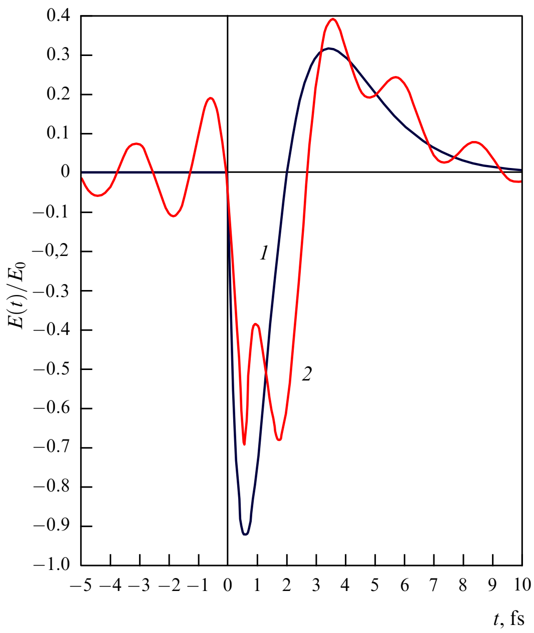

Figure 7. Fast modulation of the video pulse (15) and formation of superluminal precursors during tunneling through a gradient barrier; *1* and *2* are the time envelops of the incident and transmitted pulses ($t_0 = 0.5$ fs). Superluminal precursors are formed at the leading edge of the video pulse ($t < 0$).

where t_0 is the characteristic time scale, is presented in Fig. 7.

Speaking of superluminal precursors, note that the question about the tunneling rate became a sticking point in the tunneling theory beginning already in Gamow's time. Thus, the attempt by Condon and Morse [7] to calculate, using this theory, the velocity or the flight time of a particle in the region where the particle energy E is smaller than the potential barrier height U_0 revealed the principal problem: how to determine these quantities in the 'classically forbidden' region, where the particle momentum should be treated as an imaginary quantity? A year later, MacColl [8] concluded that "a wave packet moving inside a barrier exhibits no delay". Later on, the concept of the complex time attracted attention in the analysis of the fundamental-mode tunneling in a metal waveguide through a region with a lower cutoff frequency [9]. According to this concept, the tunneling time τ in the problem under study was expressed in terms of the complex transmission function $T = |T| \exp(\mathrm{i}\phi_{\mathrm{t}})$:

$$\tau = \sqrt{\left(\frac{\partial \phi_{\mathrm{t}}}{\partial \omega}\right)^2 + \left(\frac{\partial \ln |T|}{\partial \omega}\right)^2}\,. \qquad (16)$$

On the threshold of the centenary of the special theory of relativity (2005), new formulations of the causality principle, including tunneling effects, also appeared. For example, the output energy flux from a stationary medium at any instant cannot exceed the flux that would be present in the absence of the medium [10]. However, this formulation leads to contradictory judgements [11, 12], and the question of defining the tunneling time remains open.

4. Conclusions

Speaking about the controllable dispersion of waves in gradient media, it is worthwhile noting a number of its features which can be used for the development of gradient structures for optoelectronics:

(1) To produce a gradient wave barrier in the specified spectral range, an artificial material can be utilized with the absorption spectrum lying far from the strong dispersion region, unlike the absorption spectra of natural materials, which are usually located close to the strong dispersion region.

(2) The appearance of the controllable cutoff frequency in gradient dielectrics opens up the possibility of using such dielectrics instead of metal films in photonic crystal elements and other devices in plasmonics.

(3) The universal character of the above-mentioned effects based on the exact analytical solutions of Maxwell's equations for inhomogeneous media allows one to extend the obtained results to other spectral regions, for example, the gigahertz range. This analogy permits the parallel development and simulation of subwave optical, gigahertz, and quantum structures with such sets of parameters which are not encountered in natural materials.

Notice also that the formation mechanism of superluminal pulse precursors during tunneling through gradient photonic nanobarriers has been described here by exact analytical solutions of Maxwell's equations and does not require new physical hypothesis. Moreover, the use of weakly decaying tunneling modes eliminates the problem of recording exponentially decaying modes in conventional tunneling experiments. In this situation, tunneling experiments in optical and microwave regions of electromagnetic waves become decisive [13]; as pointed out above, the transmitted pulse, in which the envelope experiences a superluminal pulse shift in some part due to tunneling, has nothing in common with the incident pulse (the energy of the transmitted pulse is lower and its duration is longer than those of the incident pulse, and the temporal and spectral envelopes of these pulses are different), so that the Einstein treatment of the speed of light in vacuum as the limiting speed of motion of any object in a free space ("the speed of light in vacuum cannot depend on the source velocity" [14]) is not violated in the tunneling picture under study. However, the study of the superluminal pulse advance of some part of the pulse compared to the same pulse propagating in vacuum can be of not only academic but also practical interest, opening new possibilities for applications.

Acknowledgments

The authors thank T Arecci, L M Zelenyi, M A Zuev, V Kuzmiak, A A Maradudin, G Petite, O V Rudenko, and V E Fortov for useful discussions of the results of this paper.

References

1. Gamow G *Z. Phys.* **51** 204 (1928)
2. Shvartsburg A B *Usp. Fiz. Nauk* **177** 43 (2007) [*Phys. Usp.* **50** 37 (2007)]
3. Shvartsburg A B, Kuzmiak V, Petite G *Phys. Rep.* **452** 33 (2007)
4. Shvartsburg A B, Petite G, Zuev M *J. Opt. Soc. Am. B* **28** 2271 (2011)
5. Ginzburg V L *Rasprostranenie Elektromagnitnykh Voln v Plazme* (The Propagation of Electromagnetic Waves in Plasmas) (Moscow: Nauka, 1967) [Translated into English (Oxford: Pergamon Press, 1970)]
6. Shvartsburg A B *Impulse Time-Domain Electromagnetics of Continuous Media* (Boston: Birkhäuser, 1999)
7. Condon E U, Morse P M *Rev. Mod. Phys.* **3** 43 (1931)
8. MacColl L A *Phys. Rev.* **40** 621 (1932)

9. Buttiker M, Landauer R *J. Phys. C Solid State Phys.* **21** 6207 (1988)
10. Steinberg A M, Kwiat P G, Chiao R Y *Phys. Rev. Lett.* **71** 708 (1993)
11. Nimtz G, Enders A, Spieker H *J. Physique I* **4** 565 (1994)
12. Milonni P W *J. Phys. B At. Mol. Opt. Phys.* **35** R31 (2002)
13. Shvartsburg A B et al. *Phys. Rev. E* **78** 016601 (2008)
14. Einstein A "On the electrodynamics of moving bodies", in *The Collected Papers of Albert Einstein* Vol. 2 *The Swiss Years: Writings, 1900 – 1909* (Eds J Stachel et al.) (Princeton, N.J.: Princeton Univ. Press, 1989)

PACS numbers: **43.20.+g**, **43.30.+m**, **43.60.–c**
DOI: 10.3367/UFNe.0181.201111k.1217

Focusing of low-frequency sound fields on the ocean shelf

V G Petnikov, A A Stromkov

1. Introduction

The utility of focused low-frequency (100–500 Hz) sound for solving a variety of applied tasks of sea-shelf acoustics is presently a subject of ongoing research. The case in point concerns focusing of sound waves at distances of several dozen kilometers from focusing systems in a sea with a typical depth of 100 m.

From a physical viewpoint, the question to be answered is how to focus sound waves in a planar waveguide, the parameters of which (depth, refractive index, and acoustic characteristics of the lower boundary set by the oceanic bottom) are some complex functions of space coordinates. It is essential that part of these parameters, primarily the refractive index, exhibit random fluctuations in space and time. Furthermore, the distance to the focal point far exceeds the size of the focusing system.

Under these circumstances, perhaps the only way to focus sound waves consists in adopting methods based on the generation by the focusing system of a wave field that is conjugate to the medium. Such methods include the wave front reversal (WFR) (or phase conjugation) of sound waves and a similar approach based on time wave reversal [1–3], dubbed the time-reversal mirror (TRM). It should be kept in mind that both methods rely on detecting sound waves emitted by a probe source (PS) placed at the supposed focal point and subsequent generation of the reversed wave field by the focusing system backwards into the waveguide. Sound propagation in the opposite direction through just the same inhomogeneities as encountered on the direct way leads to the compensation of phase and time distortions of the acoustic signals and, as a result, to focusing on the PS site.

This paper describes methods and research results related to unusual properties of focused sound in shallow water. It discusses characteristics of physical setups designed for focusing sound waves in conditions that are very experimentally demanding. It also considers possible areas where the focused sound can be utilized.

V G Petnikov A M Prokhorov General Physics Institute, Russian Academy of Sciences, Moscow, Russian Federation
E-mail: petniko@kapella.gpi.ru
Stromkov A A Institute of Applied Physics, RAS, Nizhny Novgorod, Russian Federation

Uspekhi Fizicheskikh Nauk **181** (11) 1217 – 1222 (2011)
DOI: 10.3367/UFNr.0181.201111k.1217
Translated by S D Danilov; edited by A Radzig

2. Methods of the investigation of focused sound in shallow water

Studies of specific features of sound focusing in ocean shelf have been carried out both through numerical simulations and on-site experiments (see, for example, Refs [4–6]). Generally, the TRM-based focusing effect in some vicinity of point $\mathbf{r}_0$ was computed for the spatial distribution of the quantity $B(\mathbf{r})$:

$$B(\mathbf{r}) = \max_t \big(B_c(\mathbf{r}, t)\big) = \max_t \left[\frac{1}{T}\left|\int_{-\infty}^{\infty} P(\omega, \mathbf{r})\, s(\omega) \exp(-\mathrm{i}\omega t)\, \mathrm{d}\omega\right|\right]. \tag{1}$$

The function $B_c(\mathbf{r}, t)$ represents here the envelope of the cross-correlation function of the transmitted and received retransmitted signals, which can, strictly speaking, be defined for broadband signals of finite duration; the maximum is sought with respect to time t; $\mathbf{r}_0$ is the radius vector of the focal point (the point where the PS is located); $s(\omega)$ is the spectrum of the transmitted signal; T is its duration, and $P(\omega, \mathbf{r})$ is the spectrum of the retransmitted signal at some point $\mathbf{r}$:

$$P(\omega, \mathbf{r}) = \sum_j^J Z_1(\omega, \mathbf{r}_j, \mathbf{r})\, Z^*(\omega, \mathbf{r}_0, \mathbf{r}_j)\, s^*(\omega), \tag{2}$$

with the asterisk $*$ denoting a complex conjugation. Here, $Z(\omega, \mathbf{r}_0, \mathbf{r}_j)$ and $Z_1(\omega, \mathbf{r}_j, \mathbf{r})$ are the waveguide transfer functions between points $\mathbf{r}_0$ and $\mathbf{r}_j$, and $\mathbf{r}_j$ and $\mathbf{r}$, respectively, and, finally, $\mathbf{r}_j$ is the radius vector of transceivers (receiving and emitting elements) of the focusing system. It is assumed that the role of such a system is played by a discrete vertical antenna composed of J transceivers (just such antennae are used in conventional hydroacoustic on-site experiments to transmit and receive low-frequency hydroacoustic signals).

When applied to the focusing of a quasiharmonic sound field of frequency $\omega = \omega_0$ and arbitrarily long duration, formula (1) converts to the well-known expression for the field amplitude at the observation point:

$$P_a(\omega_0, \mathbf{r}) = \left|\sum_j^J Z_1(\omega_0, \mathbf{r}_j, \mathbf{r})\, Z^*(\omega_0, \mathbf{r}_0, \mathbf{r}_j)\right| s_0. \tag{3}$$

Formula (3) describes focusing with the help of WFR for a harmonic PS with the amplitude s_0. As shown by Zverev [3], the two methods of focusing (based on WFR and TRM) possess principal distinctions, which has just been corroborated by numerical modeling.

In numerical simulations, the transfer functions were taken as sums of interacting waveguide modes. In particular, the following expression served to compute the $Z(\omega, \mathbf{r}_0, \mathbf{r}_j)$ function:

$$Z(\omega, \mathbf{r}_0, \mathbf{r}_j) = \sum_m^{M(\omega)} C_m(\omega, \mathbf{r}_0, \mathbf{r}_j)\, \frac{\psi_m(\omega, z_j)}{\sqrt{q_m(\omega) r_0}} \exp\big(\mathrm{i} q_m(\omega) r_0\big), \tag{4}$$

where $\psi_m(\omega, z)$ and $\xi_m(\omega)$ are the eigenfunctions (waveguide modes) and eigenvalues of the related Sturm–Liouville problem $[\xi_m(\omega) = q_m(\omega) + \mathrm{i}\gamma_m(\omega)/2]$, respectively, and $M(\omega)$ is the number of propagating modes. The expression for $Z_1(\omega, \mathbf{r}_j, \mathbf{r})$ is written out in a similar way [6].

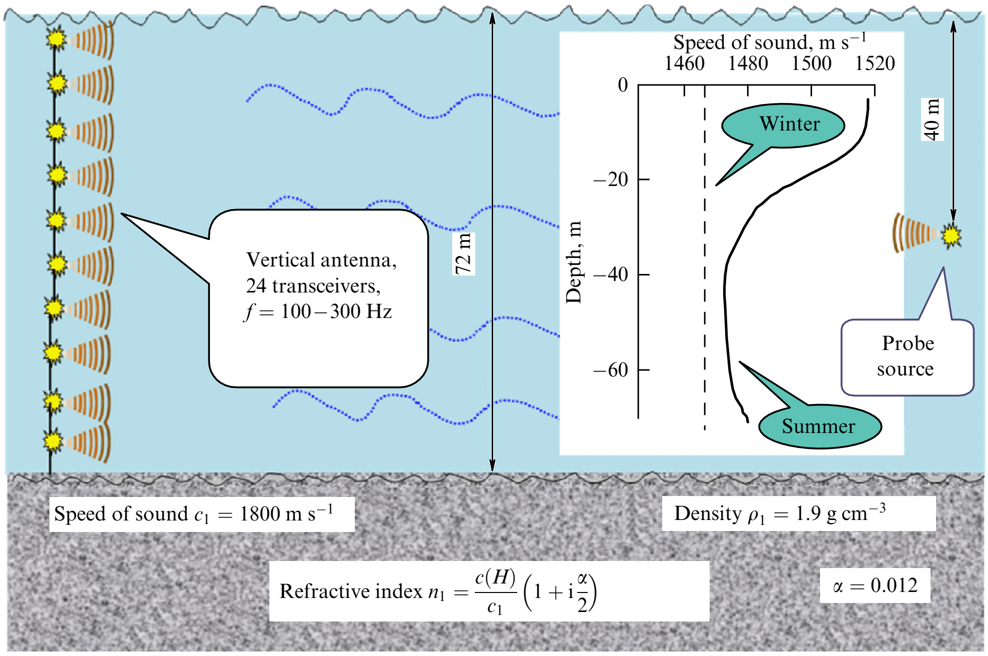

Figure 1. Schematics and parameters of numerical modeling.

The coefficients $C_m(\omega, \mathbf{r}_0, \mathbf{r}_j)$ are found by solving the system of differential equations for interacting modes in the range of distances from the probe source to the receiving–transmitting element of the antenna [6]. The key aspect of these equations is the coefficient of intermodal interaction, which depends on the form of space–time perturbations of the refractive index (the speed of sound) in the waveguide. On the sea shelf, these perturbations are primarily brought about by surface waves and, during the summer season, also by internal-gravity waves.

Modeling of a sound field focusing involves the solution of a more general problem on the interaction of waves of different natures on the oceanic shelf. The solution method was proposed in Ref. [7]. We only mention here that this method exploits the spatio–temporal power spectra of random vertical fluid displacements in the field of gravity and surface waves. For the field of background internal waves in the shelf zone, such spectra (noticeably varying among ocean sites) are measured in experiments including radar observations of surface manifestations of internal waves. For the surface waves, one may apply the known empirical relationships for the wind waves spectrum (for example, the Neyman–Pearson relationship).

Thus, by using relationships (1) and (3), it appears possible to compute the focused sound field in the vicinity of the probe source with a TRM and a WFR. Of primary interest is the field calculation in the vertical plane passing through the focusing antenna and the PS. In a cylindrical reference frame centered at the antenna, this is the (r, z, φ_0) plane, where r is the distance, z is the depth, and φ_0 is the angle specifying direction to the source. The noteworthy feature of this problem — also the one of practical significance — is the fact that in a horizontally homogeneous waveguide in the absence of random perturbations (for example, under calm weather conditions in winter), focusing occurs in any vertical (r, z, φ) plane, and not only in the PS plane, provided, certainly, that the waveguide parameters are independent of φ. Put differently, the focal region in this case looks like a torus. Admittedly, this case in not a typical one. More probable is the situation where a weak dependence of the waveguide parameters on the angle φ still exists, and the focal region takes the form of a toroidal segment.

Given modern computational capabilities, the calculation of a focused sound field in the (r, z, φ_0) plane with the required spatial resolution does not face practical difficulties. Figure 1 shows the schematics and parameters of a numerical experiment on sound focusing in a typical ocean shelf region, the results of which are described in Section 3. Their salient features, mentioned below, were tested and observed by us in numerical simulations spanning a sufficiently broad range of parameters (not only those of Fig. 1) characteristic of the focusing problem in a shallow water.

In contrast, measurements of spatial characteristics of a sound field in the (r, z, φ_0) plane are hardly possible under natural conditions. This would require the deployment of a large number of vertical receiver arrays in this plane. Under the assumption that the PS shares its location with one of the receivers in these arrays ($r_0 = r_{q'}$, $z_0 = z_{n'}$), formulas (1) and (3) can be rewritten as

$$B(r_q, z_n) = \max_t \left[\frac{1}{T} \left| \int_{-\infty}^{\infty} \sum_j^J Z_1(\omega, z_j, r_q, z_n) \times Z^*(\omega, r_{q'}, z_{n'}, z_j) \left| s(\omega) \right|^2 \exp(-\mathrm{i}\omega t)\, \mathrm{d}\omega \right| \right], \quad (5)$$

$$P_{\mathrm{a}}(\omega_0, r_q, z_n) = \left| \sum_j^J Z_1(\omega_0, z_j, r_q, z_n)\, Z^*(\omega_0, r_{q'}, z_{n'}, z_j) \right| s_0 \,. \quad (6)$$

The spatial resolution and size of the tested domain will be determined by the number of arrays and the distance between the receivers.

At present, the results of on-site experiments with only one array are available [4], which has enabled one to

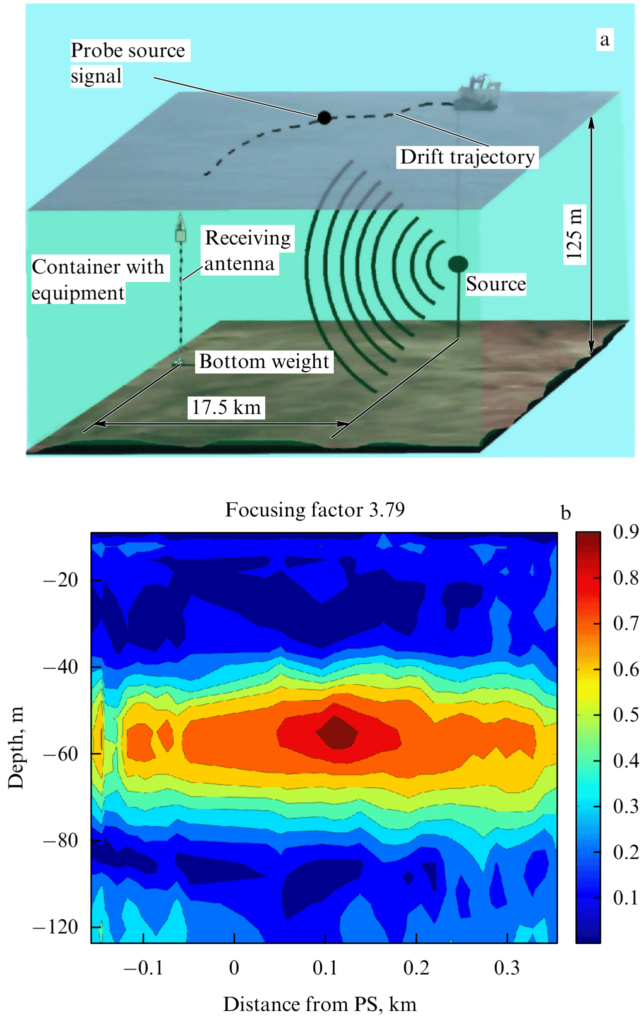

Figure 2. (a) Schematics and parameters of the on-site experiment in the Barents Sea. (b) Focusing of sound field in the frequency range 100–300 Hz.

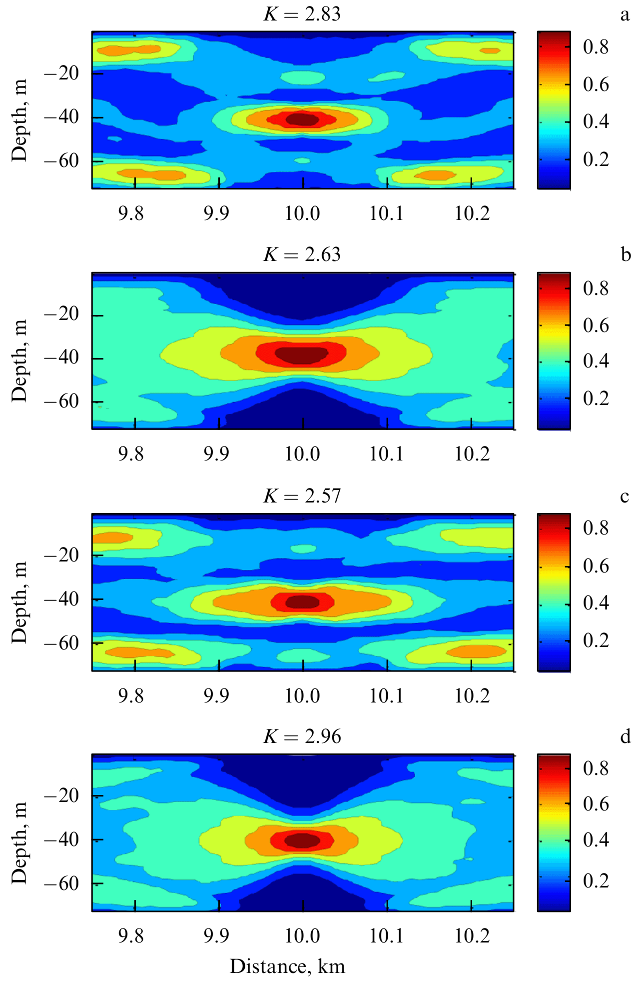

Figure 3. Focusing of the sound field by using TRM (numerical simulations): a single transceiver at a depth of (a) 9 m, (b) 40 m, and (c) 63 m; (d) focusing vertical antenna.

measure the vertical distribution of sound pressure in the focal spot and its evolution with time. This experiment, however, was carried out in a closed sea-shelf region characterized by gentle stratification and weak surface waves, i.e., in the absence of random perturbations in the sound speed profile. Under these circumstances, i.e., in the approximation of a 'frozen' medium, there exists a simpler technique of assessing the quality of focusing, implemented in our experiments [5]. We mean a combined method of estimating the quality of focusing, which incorporates measurements of waveguide transfer functions and subsequent computation of the focused sound field. Naturally, the reversibility of the transfer function with respect to exchanging the source and sound receiver is assumed to be granted.

The measurement technique is schematically illustrated in Fig. 2 which depicts a research vessel towing a source of sound toward the receiving antenna. The towing track, which passes through the supposed sound focal point, is located in the (r, z, φ_0) plane. Recording the known signal from the sound source enables the transfer functions $Z(\omega, r_0, z_0, \varphi_0, z_j)$ and $Z_1(\omega, z_j, r_q, z_{n'}, \varphi_0)$ to be measured and then, using Eqns (5) and (6), the sound field distribution over the focal spot to be computed.

3. Specific features of sound focusing on sea shelves

Specific features of low-frequency sound focusing in shallow water stem from the waveguide character of sound field propagation. First and foremost among them, we should mention the possibility of focusing with the help of a single transceiver if the TRM is applied and a broadband acoustic field is induced.[1]

Figure 3 demonstrates an example of such focusing (hereinafter we consider the distribution $B(r, z)$ normalized on its maximum value) at a distance of $\approx$ 10 km. In modeling it was assumed that the probe source emits a signal with a linear frequency modulation in the band $f = 100-300$ Hz. As a rough estimate of focusing quality, Fig. 3 also shows the computed value of the coefficient $K = \max(B(r, z))/\langle B(r, z)\rangle$ commonly referred to as the focusing factor.[2] Here, $\max(B(r, z))$ implies the maximum value of the quantity $B(r, z)$ varying over the ranges of r and z specified in Fig. 3, and $\langle B(r, z)\rangle$ is the mean value over those intervals excluding the focal point.

[1] Thus, focusing in a waveguide is analogous to that with the help of a single transceiver in a strongly scattering medium [2].

[2] Notice that for focusing quasiharmonic sound fields with the help of the WFR, we can similarly write out the expression for K which will feature $P_a(r, z)$ instead of $B(r, z)$.

As can be seen from Fig. 3, the quality of focusing provided by the vertical antenna is only slightly better than that offered by a single transceiver. The quantity K, however, does not reflect certain aspects of focusing procedure. For example, the character of focusing for a single transceiver depends on the depth. If the transceiver is placed at the same depth z_0 as the PS, the sound field is concentrated in the region of the focal spot, although the spot size is somewhat larger than with the vertical antenna. If the transceiver is located in some proximity to the waveguide boundaries, the size of the focal spot is approximately the same as for the vertical antenna. However, in such cases the field distribution is characterized by side maxima, which are absent when the transceiver is located at z_0 or if the antenna is used. These peculiarities are caused by the dependence of the excited mode spectrum on the depth of the sound source immersion.

The feasibility of focusing with the help of a single transceiver was also confirmed by computations that utilized transfer functions measured in a real experiment (see Fig. 2). The bandwidth of transmitted acoustic signals was $f = 100$–300 Hz. Computations of the focused field were performed by a formula for a single transceiver located at the depth z_j [5]:

$$B(r_q, z_n) = \max_t \left[\frac{1}{T} \left| \int_{-\infty}^{\infty} Z(\omega, r_q, z_{n'}, z_n) \right.\right.$$
$$\left.\left. \times Z^*(\omega, r_{q'}, z_{n'}, z_j) \left| s(\omega) \right|^2 \exp(-\mathrm{i}\omega t)\, \mathrm{d}\omega \right| \right], \tag{7}$$

where $n = 1, 2, \ldots, J$. Formula (7) coincides with the exact expression (5) only for points lying at the trajectory of sound source motion in the on-site experiment. Nevertheless, numerical results indicated that this formula correctly describes sound focusing in the (r, z, φ_0) plane.

We also emphasize that the quality of focusing for a single transceiver and the TRM essentially depends on the relative bandwidth $\Delta f/f$ of the sound field. Numerical simulations indicated that, under typical conditions of shallow water, the magnitude of $\Delta f/f$, which keeps the focusing factor above 2.5, exceeds 40%.

When employing WFR, focusing of the sound field with the help of a single transceiver becomes impossible. In this case, one needs to apply extended vertical antennae spanning the entire depth of the shallow water waveguide. Figure 4 demonstrates the results of focusing with a WFR at different frequencies for harmonic acoustic signals [computations rely on Eqn (6)]. As could be anticipated, the quality of focusing rises when the frequency increases. The comparison of Figs 3 and 4 gives evidence that the quality of focusing with the TRM and WFR is largely similar provided that the WFR of acoustic waves with frequency $f = 200$ Hz is used, i.e., the frequency which is equal to the mean frequency of linear-frequency-modulated (LFM) signals utilized for the TRM.[3] It turned out simultaneously that the quality only weakly depends on the number of transceivers for the same total length of focusing antenna (Fig. 4b, d). Conversely, the quality of focusing sharply drops if the length of the antenna is reduced but the number of transceivers is preserved. The fact that the separation between transceivers becomes decreasingly smaller compared to $\lambda/2$ (λ being the wavelength of sound) does not lead to a substantial impact. In particular, the results of computations indicate the absence of any focusing if the antenna length $L \leqslant 0.2H$ (H is the waveguide depth) and if the depth of immersion of the antenna phase center noticeably differs from that of the probe source. Noteworthy, all these effects derive from the waveguide's sound propagation.

The size of the focal spot in the (r, z, φ_0) plane depends on the distance r to the focusing system, this dependence, however, being weak compared to the similar dependence for the domain of vertical wave field localization in the free space, as provided by a linear vertical antenna ($D_\perp \approx r\lambda/L$). The size of the focal spot also depends on the number M of energy-carrying waveguide modes at the site of the probe sound source. Because of sound damping, the effective number M of modes reduces with the distance, and the size of the focal spot increases. For the waveguide sketched in Fig. 1, Table 1 lists the sizes of focal spots (on the level of 0.7)

[3] Here, we compare the quality of focusing achieved with one and the same antenna.

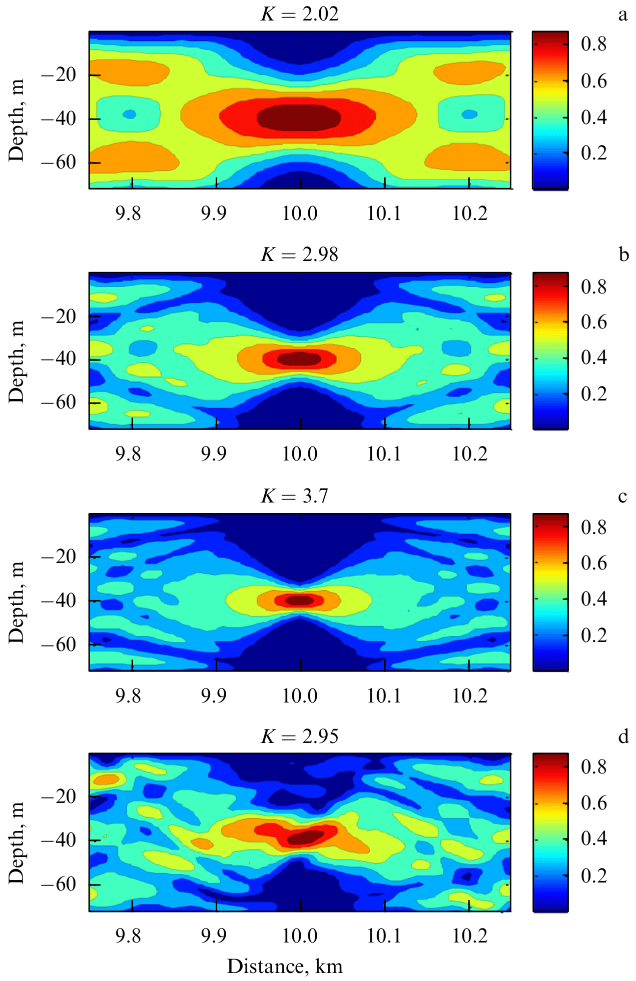

Figure 4. Focusing of the sound field by using WFR (numerical simulations): (a) $f = 100$ Hz, 24 transceivers; (b) $f = 200$ Hz, 24 transceivers; (c) $f = 300$ Hz, 24 transceivers, and (d) $f = 200$ Hz, 5 transceivers.

Table 1

Spot size, m / Distance r, km	$D_\perp$	$D_\parallel$
10	10.3	104
30	18.8	410

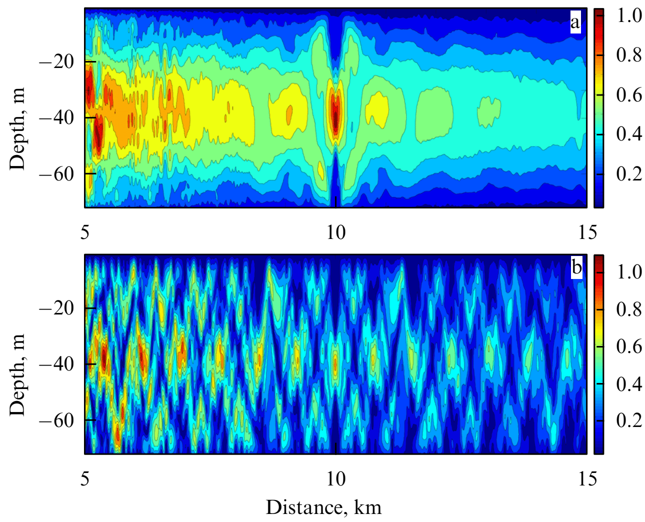

Figure 5. The interference structure of focused acoustic radiation in a shallow-water waveguide. The PS resides at the distance of 10 km, and depth of 40 m. (a) TRM with a single transceiver at the point $r = 0$ and $z_j = 40$ m. (b) WFR with the focusing antenna spanning the total depth at the origin of the coordinates.

computed with the help of formula (6). Here, $D_\perp$ and $D_\|$ are the vertical and horizontal focal spot sizes, respectively. The sound radiation frequency is $f = 200$ Hz.

The focused field behaves in a specific way not only in the vicinity of PS. In fact, focusing reshapes the interference patterns of the sound field throughout the waveguide. The emerging interference structure (it is referred to as the speckle structure in optics) is characterized by the formation of secondary focal spots located both before and behind the PS with respect to the focusing system. Examples of such a structure are furnished by Fig. 5 for both the TRM and WFR cases. As is apparent from the figure, the appearance effect of secondary focal spots is manifested more strongly for the WFR.

In the interval spanning several hundred meters in the horizontal plane, the position of the focal spot can be changed without resorting to repeated focusing with the help of the PS. One only needs to change the radiation frequency of the focusing antenna by several hertz, preserving the amplitude–phase distribution across its aperture. Notice that not only the position of the main focal spot, but also the positions of the secondary spots mentioned above change in this case. Thus, we get a possibility of scanning by focused sound waves.

As time progresses, spatio–temporal perturbations on the sea shelf substantially deteriorates the initially achieved acoustic field focusing. In particular, surface wind-generated waves in winter periods, when the speed of sound in the water layer depends only slightly on the depth (see Fig. 1), prevent one from getting a stable focusing at a distance of 10 km, even for the mild wind velocity, $V \approx 12$ m s^{-1} (Fig. 6). In summer, however, a warm upper layer forms over the shelf, which leads to the build-up of a near-bottom sound channel. The bottom-trapped waveguide modes that propagate in such a channel interact only weakly with the sea surface. As follows from numerical modeling, a stable focusing of sound is possible under these circumstances at a distance of several dozen kilometers for the same wind velocity $V \approx 12$ m s^{-1}. To this end, one needs to single out separate waveguide modes with the assistance of vertical

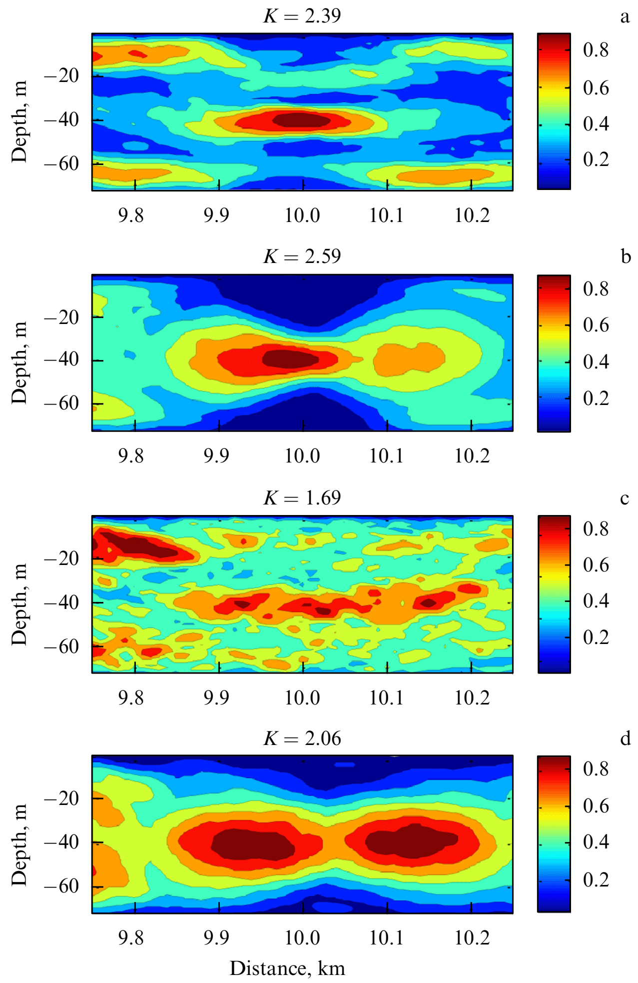

Figure 6. Focusing of sound based on the TRM in the presence of surface waves (numerical simulations): (a) $V = 9$ m s^{-1}, single transceiver at the depth of 9 m; (b) $V = 9$ m s^{-1}, focusing vertical antenna; (c) $V = 12$ m s^{-1}, single transceiver at the depth of 9 m, and (d) $V = 12$ m s^{-1}, focusing vertical antenna.

antennae and use further the sound field with a required mode composition for focusing.

Background internal waves (IWs), observed as a rule in summer, also substantially deteriorate the quality of focusing with time. This deterioration is especially noticeable in open regions of the oceanic shelf (for example, on the U.S. Atlantic Shelf or the Pacific Shelf in the vicinity of Kamchatka), where the intensity of IWs is fairly large. Numerical simulations performed with account for spatio–temporal spectra of the IWs observed in these regions have shown that already at the distance of 20 km the focal spot spreads out and 'leaves' the location of the PS under the action of internal waves. Such modifications in the focal spot happen as the IW field correlation time elapses, which takes several hours.

4. Conclusions

In summary, the focused acoustic field in ocean shelf waters exhibits a set of rather unusual physical properties which lay the basis for its wide practical implementation. We list briefly the areas where the focused sound can be applied:

• large-scale acoustical monitoring of the ocean shelf based on measurements of frequency shifts of the sound field interference maxima (including those formed because of focusing) in the frequency domain [8];

• far acoustic underwater communications, for which the focusing not only provides an advantageous signal/noise ratio at the reception point, but also ensures effective suppression of multipath reception [9];

• the acoustic tomography of shallow water, in which case the long-range reverberation can be suppressed owing to focusing [10, 11].

The authors' research results presented in this report were obtained with support from the RFBR (projects 08-02-00283, 10-02-01019, and 11-02-00779).

References

1. Dargeiko M M et al. *Izv. Vyssh. Uchebn. Zaved. Radiofiz.* **27** 746 (1984) [*Radiophys. Quantum Electron.* **27** 516 (1984)]
2. Fink M et al. *Rep. Prog. Phys.* **63** 1933 (2000)
3. Zverev V A *Izbrannye Trudy* (Selected Works) (N. Novgorod: IPF RAN, 2004)
4. Kuperman W et al. *J. Acoust. Soc. Am.* **103** 25 (1998)
5. Zverev V A, Korotin P I, Stromkov A A *Akust. Zh.* **54** 69 (2008) [*Acoust. Phys.* **54** 58 (2008)]
6. Lunkov A A, Petnikov V G, Stromkov A A *Akust. Zh.* **56** 256 (2010) [*Acoust. Phys.* **56** 228 (2010)]
7. Kuz'kin V M et al. *Akust. Zh.* **52** 74 (2006) [*Acoust. Phys.* **52** 65 (2006)]
8. Kuz'kin V M, Pereselkov S A *Akust. Zh.* **53** 833 (2007) [*Acoust. Phys.* **53** 736 (2007)]
9. Edelmann G F et al. *IEEE J. Ocean. Eng.* **27** 602 (2002)
10. Kim S et al. *J. Acoust. Soc. Am.* **115** 1525 (2004)
11. Pereselkov S A, Petnikov V G *Akust. Zh.* **53** 400 (2007) [*Acoust. Phys.* **53** 348 (2007)]

PACS numbers: **43.20.+g**, **43.30.+m**, 43.60.Pt
DOI: 10.3367/UFNe.0181.201111l.1222

Low-mode acoustics of shallow water waveguides

A G Luchinin, A I Khil'ko

1. Introduction

The industrial exploitation of gas and oil fields on the Arctic Shelf and in shallow marginal seas motivates creating information provision with hydroacoustic (HA) facilities aimed, among others, at the tasks of hydroacoustic communications and subsea surveillance. These tasks are usual for underwater acoustics, yet for a long time they were dealt with mainly at moderate distances (1–10 km), when utilizing high-frequency sound waves was efficient [1].

A new stage in the development of underwater acoustics was brought about by using low-frequency (LF) sound to ensure the solution of information tasks over large distances (10^3 km or more) in the deep sea. The research related to such HA systems was initiated abroad by W Munk and colleagues [2] in the 1970s. By the end of the 1970s, Soviet scientists, led by A V Gaponov-Grekhov, actively joined this research. During a short stretch of time they have contributed to the basic principles of LF underwater acoustics, created original low-frequency hydroacoustic (LFHA) transmitters, and carried out experiments in which diffracted LFHA signals have been measured in deep underwater HA channels over long observation distances on record [3].

By the end of 1980, prompted by the increasing interest in the industrial exploitation of the ocean shelf, the realization of HA-observations in extended regions of shallow seas became a pressing issue. In this case, the interaction of an HA field with the sea surface and bottom becomes essential, and, as a result, the field is strongly damped and loses coherence [4]. Moreover, the sound wave propagation is accompanied by high levels of reverberation noise [5]. These effects are the strongest for the interfering multimodal part of LFHA pulses which, as indicated by observations, is unstable in time and rapidly decays. Because of this, past endeavors relying on the usage of individual monopole sources for long-range LF sonar in shallow seas, the increase in their power, or the usage of large receiving arrays failed in providing the necessary progress to solve this problem.

2. The mode shadow and tomographic reconstruction of inhomogeneities

The idea of how to create information HA provision emerged in discussions among A V Gaponov-Grekhov, V I Talanov, V A Zverev, and V V Kovalenko in 1995–1996. Its essence reduces to utilizing only well-propagating LF waveguide (200–400 Hz) modes (in most cases they are also the lower-order modes) for acoustic background illumination of water depth in shallow seas and performing their selective detection. This approach was known in optics and radiophysics but has not been utilized in ocean acoustics.

As confirmed by estimates, such a low-mode-number field, owing to its relatively weak dissipation, should have a larger intensity than a multimode one, given the same energy delivered to the transmitting complex. Additionally, making use of low-mode HA fields could be advantageous in reducing reverberation as a whole and, in particular, the correlation noise from the direct illumination signal if one receives signals belonging to modes of other numbers (it is the shadow principle, also adapted from optics, but in this case applied to modes).

Subsequent analysis has shown that by using the complexly modulated mode pulses, matched to the waveguide, in HA observations in shallow seas it is possible not only to maintain long-distance underwater communications, but also to realize HA sonar through ultimate observation distances. In order to better resolve the underwater landscape over extended sea regions, the method of multistatic (tomographic) surveillance has been adopted, according to which the resultant object image is formed by accumulating projections.

Taking into account all the above-mentioned principles which define the concept of low-mode shallow-sea acoustics, the low-mode pulse acoustic tomography (LMPAT) method has been proposed. Its essence can be formulated as follows. With the help of a set of extended vertical arrays S_i ($i = 1, \ldots, I$), pulse signals corresponding to a particular mode number n are generated, with a sufficiently narrow uncertainty function in the 'frequency–time' parameter plane. The waveguide vertical profile and mode structure are assumed to be known.

Understandably, the excitation of an individual mode is impossible in practice because of the finiteness of the

A G Luchinin, A I Khil'ko Institute of Applied Physics, Russian Academy of Sciences, Nizhny Novgorod, Russian Federation
E-mails: Luch@hydro.appl.sci-nnov.ru, A.khil@hydro.appl.sci-nnov.ru

Uspekhi Fizicheskikh Nauk **181** (11) 1222–1228 (2011)
DOI: 10.3367/UFNr.0181.201111l.1222
Translated by S D Danilov; edited by A Radzig

transmitting array aperture and the impossibility of placing sources deep into the ocean bottom. To synthesize a desired field distribution over the transmitting aperture, it is therefore necessary that all extra emitted modes stay substantially weaker than a single mode generated in a consistent way [6, 7]. In this case, the generated signal can be considered as a low-mode-number one. The pulses scattered by an observed inhomogeneity and corresponding to modes of numbers $m = 1, \ldots, M$, where M is the total number of modes propagating in the waveguide, are detected with the help of extended vertical receiver arrays R_j $(j = 1, \ldots, J)$. For each of the modes singled out by the receiver system, the matched filtering of pulses, spanning through time delays τ and Doppler frequency shifts Ω, is performed. The number and position of sound sources and receiver systems, as well as the number of mode tomographic projections corresponding to each 'source–receiver system' pair, may vary.

As a result, signals registered for each pair of combinations of the transmitting and receiving arrays are the functions of several variables: the transmitted and detected mode numbers, and of time delays and Doppler frequency shifts.

By jointly processing all spatial mode and frequency tomographic projections, one retrieves spatial and temporal parameters of the observed inhomogeneities. Far from the source, the field in HA waveguides is given by a finite sum of N propagating modes (for a horizontally homogeneous waveguide, the numbers of modes at the locations of the source and receiver coincide and $N \equiv M$). A mode is characterized by its eigenfunction $\varphi_n(z)$ and complex-valued eigenvalue $h_n(\omega)$, whose imaginary part is determined by the mode decay decrement $\delta_n(\omega)$. Each ith source of the tomographic system, being an array of transducers of length L_i, emits a sequence of narrow-band sounding pulses $f_0(t)$ with spectrum $F(\omega - \omega_0)$, where ω_0 is the carrier frequency. If the location depths and sizes of sound source arrays are selected in an optimal way, the emitted low-mode signal will contain an emitted mode with number n, whose amplitude maximally exceeds the amplitudes of all other modes [6]. In this case, under the assumption that the intermode dispersion effects are small (this imposes limitations on the bandwidth of emitted pulses, and also on the distances through which they are observed), the direct (unscattered) pulse signal from the jth receiving array of length L_j can be written, after matched filtering, in the following form

$$
\begin{aligned}
&{}^0P_{ij}^{nm}(r_{ij}, \tau_{ij}^{nm}, \Omega_{ij}^{nm}) \\
&= A_n^i A_n^j \exp\left[\mathrm{i}\left(h_n r_{ij} - \frac{\pi}{4}\right)\right](h_n r_{ij})^{-1/2} F_{\mathrm{ind}}(\tau_{ij}^{nn}, \Omega_{ij}^{nn}) \\
&+ \sum_{\substack{\eta \neq n \\ \mu \neq m}}^{M} A_\eta^i A_\mu^j \exp\left[\mathrm{i}\left(h_\eta r_{ij} - \frac{\pi}{4}\right)\right](h_\eta r_{ij})^{-1/2} F_{\mathrm{ind}}(\tau_{ij}^{\eta\mu}, \Omega_{ij}^{\eta\mu}) , \quad (1)
\end{aligned}
$$

where $h_n = h_n(\omega_0)$; $\tau_{ij}^{nm} = r_{ij}/v_n(\omega_0)$ is the delay in the pulse pertaining to the nth mode in the receiving channel which corresponds to the mode with number m; $v_n(\omega_0)$ is the group velocity of mode n; Ω_{ij}^{nm} is the Doppler frequency shift caused by the motion of the scattering object; $A_{n,m}^{i,j} = \int_0^{L_{i,j}} g_{n,m}^{i,j}(z)\, \varphi_{n,m}(z)\, \mathrm{d}z$ are the mode excitation coefficients for the transmitting and receiving arrays, respectively; $g_{n,m}^{i,j}(z)$ are optimal weight factors along array apertures [8], and $F_{\mathrm{ind}}(\tau, \Omega)$ is the uncertainty function of the sounding pulses:

$$
F_{\mathrm{ind}}(\tau, \Omega) = \frac{1}{2\pi} \int_{-\infty}^{\infty} \mathrm{d}\omega\, F(\omega)\, F_0(\omega - \Omega) \exp\left[\mathrm{i}(\omega - \Omega)\tau\right] ,
$$

where $F_0(\omega)$ is the spectrum of the sounding signal replica.

Given ideal spatial filtering, which is not achievable under natural conditions, for which mode orthogonality conditions hold at array apertures, the second term in the form of a sum of small-amplitude interfering modes disappears on the right-hand side of Eqn (1), leaving only the first term related to the field of acoustic illumination for a single emitted mode.

In observations, one detects sounding pulses that experience diffraction by waveguide inhomogeneities. In the framework of the mode-guided description, the complex-valued amplitudes of diffracted waveguide modes are determined by the scattering matrix which depends on the internal structure, shape, and location of inhomogeneities [5–7]. Given the acoustic illumination of inhomogeneities by a pulse signal of the nth mode, the amplitude of each pulse of the diffracted mode with index m will be formed through contributions of the signals scattered on all inhomogeneities confined within the respective pulse volume, the points of which, r', satisfy the condition $|t - r_{1i} v_n^{-1} + r_{2j} v_m^{-1}| < \Delta\tau/2$, where $r_{1i} = |r_i - r'|$ and $r_{2j} = |r' - r_j|$ are the distances from the scatterer to the source and receiver, respectively. Generally, the observed inhomogeneities move, so that the scattered pulses experience the Doppler frequency shift.

For the narrow-band pulses of acoustic illumination considered here, and given the fairly small scatterer displacement velocities V_{s}, all scatterers satisfying the condition

$$
\left|\omega_0 V_{\mathrm{s}}(r')\left(v_n^{-1} \cos \alpha_i(r_i, r') - v_m^{-1} \cos \beta_j(r_j,\, r')\right)\right| < \Delta\Omega
$$

will fall into the separate channel along the Doppler shift-axis. Here, $\alpha_i(r_i, r')$ and $\beta_j(r_j, r')$ are, respectively, the angles between the direction of displacement velocity vector of an elementary scatterer at point r' and radius vectors drawn from the location point of the scatterer to the source and the receiving system. The quantities $\Delta\tau$ and $\Delta\Omega$ are determined by the width of the uncertainty function $F_{\mathrm{ind}}(\tau, \Omega)$ of sounding pulses along the time delay- and Doppler frequency shift-axes, respectively.

When performing digital signal processing, in each of 'time delay–Doppler frequency shift' planes related to the pair of the emitted mode with number n and the received one with the number m, it is possible to introduce for each source–receiver pair (i, j) the set of channels corresponding to the intervals of time delays ${}^0t_{ij}^{nm} + (l-1)\Delta\tau < \tau_{ij}^{nm} < {}^0t_{ij}^{nm} + l\Delta\tau$ and Doppler frequency shifts $(k \mp 1)\Delta\Omega < \Omega_{ij}^{nm} < k\Delta\Omega$, where $l = 1, 2, \ldots, L$ and $k = \pm 1, 2, \ldots, \pm K$ are the channel numbers, and ${}^0t_{ij}^{nm}$ are the initial values of time delays fixed for each of the tomographic projections (i, j, n, m).

After signal processing, which consists in a matched filtering of the received mode pulses, we will generally have, adopting the discretization defined above, $I \times J \times N \times M \times K \times L$ tomographic projections, the signals of which carry integral characteristics of all inhomogeneities confined within pulse volumes for each of the projections. The joint processing of signals related to these projections provides the reconstruction of differential characteristics of the observed inhomogeneities, i.e., the distribution of their parameters over the observation domain. Under the assumption that multiple scattering effects are negligible, the amplitudes of modes scattered by separate elements of the pulse volume are defined by the components of the inhomogeneity spatial spectrum, satisfying the resonance scattering condition $\mathbf{k}_{ij}^{nm} = h_n \mathbf{r}_{1i}/r_{1i} - h_m \mathbf{r}_{2j}/r_{2j}$.

The observed amplitudes of the acoustic field pressure will represent the sum of the acoustic illumination field ${}^0p_{ij}^{nm}$, the field components ${}^\sigma p_{ij}^{nm}$ and ${}^R p_{ij}^{nm}$ diffracted by the observed inhomogeneity and scattered by all interfering inhomogeneities, respectively, and also of the ocean additive noise source field ${}^N p_j^m$. In a general case, each component of the received signal should be considered as a random signal with certain inherent statistical properties.

Assuming the interference effects are small, to assess the received signal intensity, averaging is performed over statistical ensembles of respective random inhomogeneities and noises. If the random inhomogeneities are relatively mild or the length of tomographic paths is moderate, the acoustic illumination field can approximately be considered coherent. For the illumination with acoustic mode n, the intensities of signal components at the output of the matched filter, pertaining to the pulses of the mth received mode, which are diffracted by both the observed (with index σ) and interfering (with index R) inhomogeneities, are defined by the mode scattering matrix [5–7]:

$$\begin{aligned}
&({}^{\sigma,R}I_{nm}^{\nu\mu})_{ij}(\tau_{ij}^{nm}, \tau_{ij}^{\nu\mu}, \Omega_{ij}^{nm}, \Omega_{ij}^{\nu\mu}) \\
&\simeq \frac{8}{\pi h_0^2} \int_{-\infty}^{\infty} \frac{1}{r_{1i} r_{2j}} \exp\left[\mathrm{i}(h_\nu - h_n) r_{1i} + \mathrm{i}(h_\mu - h_m) r_{2j}\right] \\
&\times \int_{-\infty}^{\infty} {}^{\sigma,R}W_{nm}^{\nu\mu}\left(\frac{h_\nu + h_n}{2}\frac{\mathbf{r}_{1i}}{r_{1i}} - \frac{h_\mu + h_m}{2}\frac{\mathbf{r}_{2j}}{r_{2j}}\,;\, \omega', r'\right) \\
&\times F_{\mathrm{ind}}\left(\tau_{ij}^{nm} - \frac{r_{1i}}{v_n} - \frac{r_{2j}}{v_m}\,;\, \omega' - \Omega_{ij}^{nm}\right) \\
&\times F_{\mathrm{ind}}^*\left(\tau_{ij}^{\nu\mu} - \frac{r_{1i}}{v_\nu} - \frac{r_{2j}}{v_\mu}\,;\, \omega' - \Omega_{ij}^{\nu\mu}\right) \mathrm{d}\omega'\, \mathrm{d}^2 r', \qquad (2)
\end{aligned}$$

where h_0 is the wave number on the channel axis for the carrier frequency, and ${}^{\sigma,R}W_{nm}^{\nu\mu}(\mathbf{k}, \omega, r)$ are the appropriate components of the local spectrum of the inhomogeneity correlation function with respect to the difference variables for the sum of surface, bottom, volume, and spatially localized inhomogeneities. Integration in formula (2) is performed over the horizontal coordinates, and the location depth of inhomogeneities is taken into account in computations of the components of the local inhomogeneity spectrum [6, 7].

3. Imitating model for the adaptation to observational conditions

A tomographic reconstruction of the object image consists in estimating the values of observed parameters of a model describing the object. For a spatially localized inhomogeneity, in particular, its coordinates and shape, together with the velocity and displacement direction, may serve as the observable parameters. When wind waves constitute the object of observation, the speed and direction of the wind generating them can be among the measured parameters [5, 6].

Let us denote by the $\mathbf{p}$ vector a set of observable model parameters. The values of the $\mathbf{p}$ components are estimated by the method of statistical hypothesis testing. These hypotheses are defined by the solution of the direct diffraction problem based on *a priori* information in the form of models of the medium, the object under observation, the levels of disturbances and noises, and a model describing the configuration of the observation system. The solution corresponds to the global minimum of the residual between the vectors $\mathbf{q}$ of measured parameters and vectors $\mathbf{q}^{(\mathbf{p})}$ which correspond to the hypotheses being exhausted, for example, in the form of the Lp-norm:

$$\Psi(\mathbf{p}) \equiv \|\mathbf{q} - \mathbf{q}^{(\mathbf{p})}\|^{\eta} \to \min_{\mathbf{p}} \Psi(\mathbf{p}) .$$

The rule for taking the decision that the hypothesis for the value of vector $\mathbf{q} = \mathbf{q}^{(\mathbf{p})}$ is valid is commonly written out as $\|\mathbf{q} - \mathbf{q}^{(\mathbf{p})}\|^{\eta} < \sigma$, where the norm $\|\,.\,\|$, the exponent η, and the threshold values of σ are defined in a general case by the distribution function of the probability density of the vector of measured parameters, by the given magnitudes of the probabilities of the first- and second-order errors in taking decisions, noises, disturbances, and other factors.

The formulation and testing of hypotheses for the parameters of the object (notably, on its location in the observation domain) assume the assessment of optimal space–frequency aperture distributions [8], relevant statistics, and criteria for each tomographic projection, which are adapted to the sounding conditions. Additionally, one needs to design optimal algorithms for accumulating projections and suggest the trajectory of the solution search (hypotheses exhaustion).

To solve these tasks, an imitating computer model has been developed. It relies on oceanographic databases, physical models concerning the formation of signals and disturbances, and algorithms of partially coherent accumulation and decision-making. It is a program-algorithm complex equipped with an interactive interface [6–10]. The results of computations are presented as the observation probability distributions for the prescribed probabilities of false alarms in a given shallow sea region, depending on observation conditions (wind, currents, navigation noises, and so on).

An example of the analysis of potentialities offered by low-mode acoustics in a shallow sea is offered by simulations of a system composed of three receiver–transmitter (RT) arrays used to trace an iceberg. The arrays are located at the vertices of an equilateral triangle with a side of 100 km (the RT modules are marked by dark points in Fig. 1a). The carrier frequency of the sounding narrow-band pulses was selected to be 200 Hz. If certain observed components of the parameter vector, in particular, the iceberg speed and drift direction, are fixed, the observation reduces to estimating the iceberg location. It has been assumed in the analysis that the iceberg moves at a speed of 1.5 m s^{-1} along a set of trajectories, each making an angle of $\pi/4$ with the x-axis (Fig. 1a). The level of additive noise was taken to be 70 dB relative to 1 μPa. The power of the acoustic illumination source was selected equal to 100 W. As follows from simulation results displayed in Fig. 1b, the system's field of view is nonisoplanatic and substantially depends on observation conditions, such as the level and structure of noise and disturbances, the waveguide structure, and the motion parameters of the inhomogeneity observed. As follows from the numerical analysis, most frequently the outer boundary of the visual field is determined by additive noises, whereas the reverberation disturbance from random waveguide inhomogeneities gives rise to the inhomogeneity of the field of view in the form of regions with poor visibility.

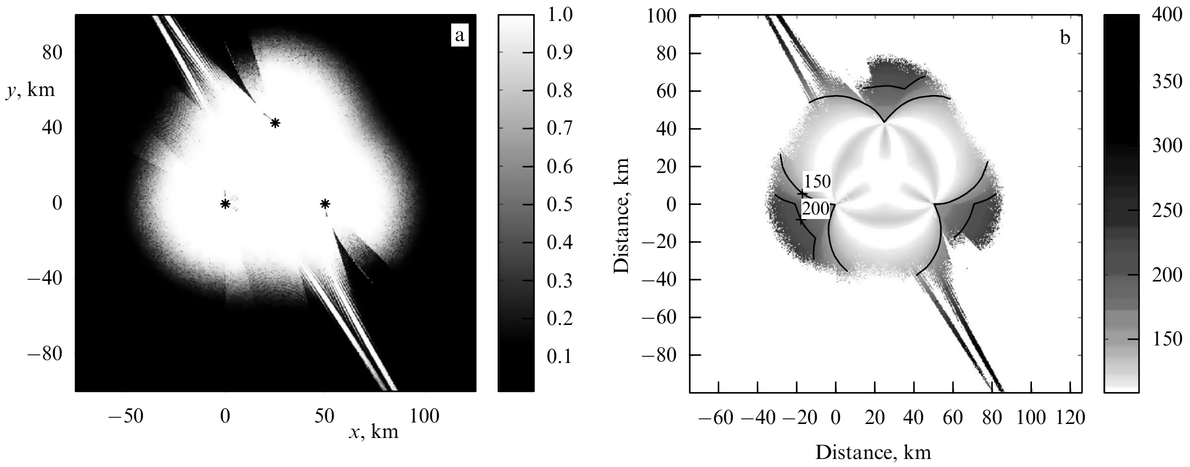

Figure 1. (a) Total field of view in the horizontal plane in the case of exciting ten mode and nine spatial projections for the noise level of 82 dB. (b) The distribution of spatial resolution values (corresponding to panel a) for the excitation of the first mode and detection of the third one. The brightness scale and spatial resolution values alongside the isolines are given in meters.

The shape of the visual field can noticeably change as a consequence of changes in the velocity and motion trajectory of the observed inhomogeneity and in the parameters of surface wind-generated waves. Notably, if the iceberg drifts along the track of bistatic observations, the regions where the bottom reverberation hampers observations will be located at right angles to the source–receiver line.

As confirmed by numerical simulations, the multistatic low-mode observation system is not limited solely to observations of spatially localized inhomogeneities, but can also tackle randomly distributed inhomogeneities, such as wind waves, and also the HA waveguide characteristics [6, 7, 9]. The results mentioned above, together with those from other studies, indicate that the ocean mode acoustics assures observations within extended zones with a minimum number of RT modules and minimum requirements imposed on the power supply.

4. Marine experiments on low-mode acoustics of shallow seas

Numerical simulations were instrumental in shaping the optimal design of a low-mode acoustic system for specific shallow-sea regions and developing the procedure of marine tests. To carry out experiments, original transmitting and receiving complexes have been designed under the supervision of B N Bogolyubov and P I Korotin. They incorporate vertically oriented transmitting and receiving LFHA arrays. In particular, by employing light and compact effective electromagnetic LF transmitters, a 16-element array with an adaptive-control system has been constructed (Fig. 2). Furthermore, unique receiving LFHA complexes have been designed, comprising hundred-meter arrays of digital hydrophones boosting a broad dynamic range and capable of working autonomously up to 7 days [6, 7]. The array aperture distributions were selected adaptively so that they conform to the array configuration which varies because of wind waves and drift, and to the hydrology. For the transmitting array, a special iterative algorithm was developed. It ensured real-time formation of mode pulses of acoustic illumination matched with the HA waveguide, with due regard for compensation of the interaction between the transmitters through the ambient medium [6, 7, 11, 12].

Figure 2. Deployment of a 16-element transmitting complex to its underwater position from the deck of the research vessel.

A set of experiments was carried out in marine conditions after creating an appropriate equipment and developing measurement procedures. They were aimed at tests of the realizability and efficiency of low-mode shallow-sea acoustics. Their outcome was, first, the demonstration of the operating capacity of equipment and the possibility of compensation of interactions among the transmitters as they emit and receive low-mode pulses (Fig. 3). The level of energy concentration for the waveguide-matched generation of the low-mode field in experiments proved to be close to the calculated one (7–10 dB). The agreement with predictions was also manifested through an essential decrease in the transition distance for arrays, compared to that for a single transmitter (Fig. 3b). Additionally, the low-mode field appeared to be much more stable in time (15–30 min) than the field due to a single source (Fig. 4).

The high coherence of signals was demonstrated by detecting low-mode pulses at large distances (in excess of 100 km). Such a peculiarity facilitated their coherent, waveguide-matched accumulation over space and frequency in the 10–20-Hz band for apertures spanning more than 1 km. Experimental demonstrations have also revealed a substan-

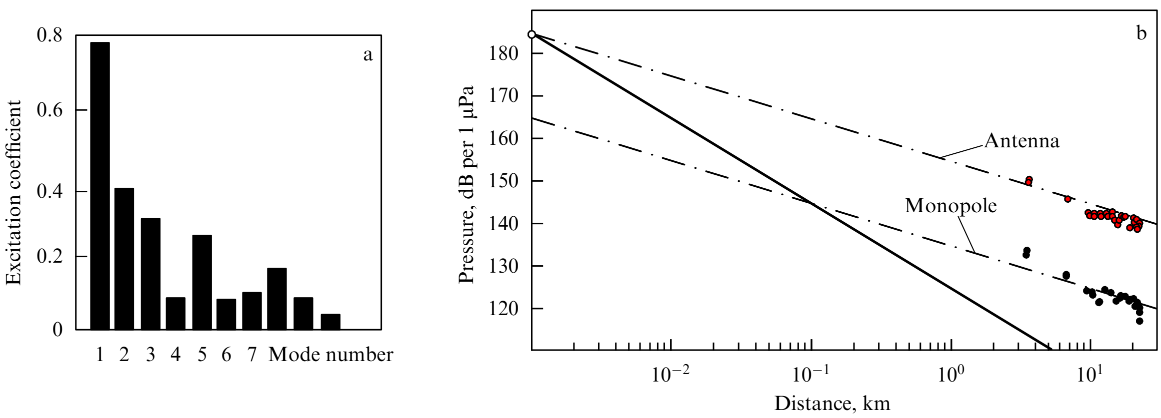

Figure 3. (a) The mode signal spectrum detected with a homogeneous amplitude–phase distribution at a distance of 10 km from the emitting array which spans the location depth range from 44 to 89 m. (b) The signal level versus distance for an emitting antenna and a monopole. The dashed-dot lines correspond to the cylindrical law of a signal level decay, and the solid line fits the spherical law. The circle on the ordinate axis marks the level of the transmitted signal which is the same for a single monopole and for an array of emitters.

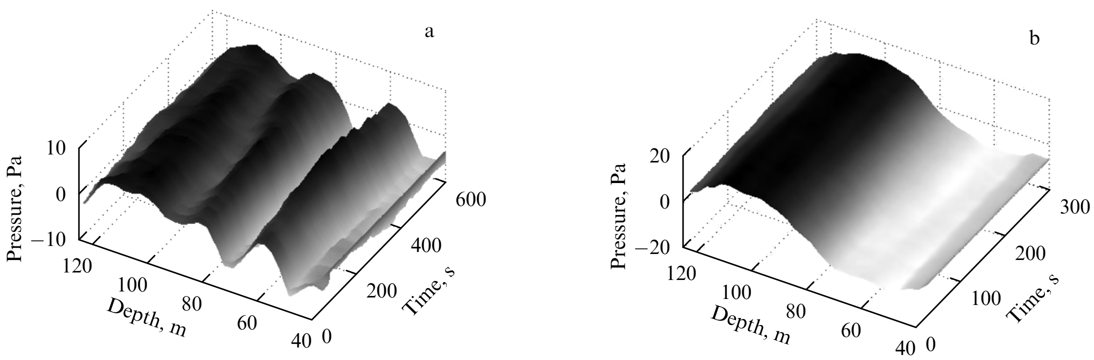

Figure 4. Sound field distribution over depth versus time, as produced by a single emitting monopole in an antenna (a), and by an antenna with a homogeneous amplitude-phase distribution over its aperture (b). The observation distance is 4 km.

tial reduction in the levels of surface and bottom reverberation (more than by 10–15 dB) with respect to the case of a single transmitter and multiple modes (Fig. 5). It was also experimentally established that the main sources of LFHA noise are distant storms and navigation — concerning low-mode-number fields — and wind-generated waves affecting more those modes with larger numbers. It was shown both in simulations and experiments that the reduction in the size of arrays leads to an essential (more than a few orders of magnitude) decrease in the area of a zone of consistent observations [6–9].

5. Conclusions

As a result, the research work described here laid the foundations of a new technology offering effective multistatic observations in shallow seas. This technology can be considered as the basis for applications in Russian shelf seas, in particular, on the Arctic Shelf. The further advancement of this technology is linked to the potential of its usage as a component in autonomous or deployed receiving–transmitting modules and elements of underwater acoustic communications. Also of importance is the research aimed at the design of adaptive observation algorithms relying on cognitive methods.

Two fields of fundamental and applied research are of key significance for the further development and practical implementation of low-mode acoustic methods. The first involves the design and construction of new, more efficient, light and compact LFHA transmitting systems. This area envisages the search for new materials and generation principles of LFHA fields. The second key area is, in our opinion, the elaboration of methods and algorithms for adaptive automated control of the potential inherent in the observation system. The main idea here is physical and technological principles needed for creating a control system that will provide automated generation of hypotheses by the imitating system in the course of observations, with allowance made for hydroacoustical conditions.

The aforementioned critical technologies offer solutions to a set of fundamental scientific problems occurring in studies of shallow regions of the world's oceans. These technologies can also be utilized in adjacent branches of science. An example is furnished by coherent seismoacoustic profiling used in searching for natural resources on the ocean bottom. In this case, one applies highly coherent LFHA transmitters, which ensures that the accumulation over space and frequencies of bottom-reflected signals is coherent and matches the ambient medium. This helps achieve a unique efficiency in reconstruction of deeply located bottom inhomogeneities, while conforming the requirements imposed by ecological security of HA sounding [13].

Acknowledgments. This work was supported through the program of the Presidium of the RAS, 'Fundamental

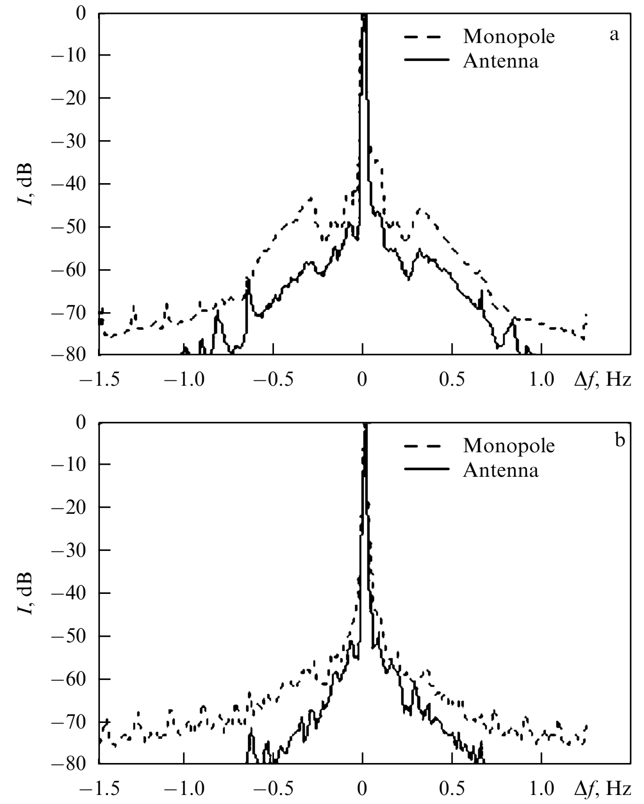

Figure 5. Spectra of intensity I of a signal generated by a monopole and an array of transmitters, which is scattered by surface wind-generated waves, at a distance of 10 km: (a) the spectrum of the total signal at the antenna, and (b) the spectrum of the first waveguide mode.

problems in oceanography: geology, physics, biology, ecology'; the program of the Physical Sciences Division of the RAS, 'Fundamental principles of acoustical sounding of artificial and natural media'; the Federal Targeted Program, 'Scientific and scientific-pedagogical personnel of innovative Russia' (contract 02.740.11.0565), and RFBR (project 09-02-00044).

References

1. Urick R J *Principles of Underwater Sound* (New York: McGraw-Hill, 1975) [Translated into Russian (Leningrad: Sudostroenie, 1978)]
2. Munk W, Worcester P, Wunsch C *Ocean Acoustic Tomography* (Cambridge: Cambridge Univ. Press, 1995)
3. Abrosimov D I et al. *Dokl. Akad. Nauk SSSR* **299** 477 (1988) [*Sov. Phys. Dokl.* **33** 123 (1988)]
4. Katsnelson B G, Petnikov V G *Akustika Melkogo Morya* (Shallow Water Acoustics) (Moscow: Nauka, 1997) [Translated into English (London: Springer, 2002)]
5. Goncharov V V et al. *Akusticheskaya Tomografiya Okeana* (Acoustic Tomography of Ocean) (N. Novgorod: IPF RAN, 1997)
6. Luchinin A G, Khil'ko A I *Akust. Zh.* **51** 228 (2005) [*Acoust. Phys.* **51** 182 (2005)]
7. Khil'ko A I et al. *Akust. Zh.* **53** 437 (2007) [*Acoust. Phys.* **53** 381 (2007)]
8. Smirnov I P, Khil'ko A I, Romanova T V *Izv. Vyssh. Uchebn. Zaved. Radiofiz.* **51** 50 (2008) [*Radiophys. Quantum Electron.* **51** 45 (2008)]
9. Khil'ko A I et al., in *Akusticheskie Izmereniya i Standartizatsiya. Ul'trazvuk i Ul'trazvukovye Tekhnologii. Atmosfernaya Akustika. Akustika Okeana. Sbornik Trudov XXII Sessii Rossiiskogo Akusticheskogo Obshchestva i Sessii Nauchnogo Soveta po Akustike RAN* (Acoustic Measurements and Standardization. Ultrasound and Ultrasonic Technologies. Atmospheric Acoustics. Ocean Acoustics. Collection of Papers of the XXIIth Session of the Russian Acoustical Society and Scientific Council on Acoustics, RAS) Vol. 2 (Moscow: GEOS, 2010) p. 244
10. Raevsky M A, Khil'ko A I *Izv. Vyssh. Uchebn. Zaved. Radiofiz.* **50** 20 (2007) [*Radiophys. Quantum Electron.* **50** 18 (2007)]
11. Averbakh V S et al. "Ob upravlenii gruppoi vzaimodeistvuyushchikh akusticheskikh monopolei" ("On the control of the group of interacting acoustic monopoles") Preprint No. 190 (Gor'ky: IPF AN SSSR, 1988)
12. Smirnov I P, Smirnova I R, Khil'ko A I *Akust. Zh.* **56** 813 (2010) [*Acoust. Phys.* **56** 1067 (2010)]
13. Lazarev V A et al., in *Fizicheskie, Geologicheskie i Biologicheskie Issledovaniya Okeanov i Morei* (Physical, Geological, and Biological Studies of Oceans and Seas) (Exec. Ed. S M Shapovalov) (Moscow: Nauchnyi Mir, 2010) p. 300

PACS numbers: **43.25.+y**, **43.30.+m**, 87.50.Y
DOI: 10.3367/UFNe.0181.201111m.1228

Developments in physical acoustics 2010: a review of materials from the Scientific Council on Acoustics of the Russian Academy of Sciences

I B Esipov

One of the tasks of the Scientific Council on Acoustics, RAS is to inform the scientific community of the most interesting results obtained in investigations performed in laboratories of the Russian Academy of Sciences and leading universities and research institutions in Russia. The Council comprises a number of sections discussing the development of investigations in the following fields:

(i) *ocean acoustics* (A G Luchinin, Head, Institute of Applied Physics, RAS);

(ii) *geoacoustics* (A V Nikolaev, Head, Shmidt Institute of Earth Physics, RAS);

(iii) *aeroacoustics* (V F Kop'ev, Head, Central Aerohydrodynamic Institute);

(iv) *vibroacoustics* (Yu I Bobrovnitskii, Head, Blagonravov Institute of Machine Science, RAS);

(v) *physical acoustics of solids and acoustoelectronics* (I E Kuznetsova, Head, Saratov Division, Kotel'nikov Institute of Radioengineering and Electronics, RAS);

(vi) *physical ultrasound* (O A Sapozhnikov, Head, Physics Department, Lomonosov Moscow State University).

As follows from the topics of these sections, the Scientific Council focuses on studies in the field of physical acoustics and its applications in related fields, such as Earth and engineering sciences.

The research activity of the Scientific Council on Acoustics, RAS in 2010 was summarized at two sessions held at the Prokhorov General Physics Institute (GPI RAS) and at the Kotel'nikov Institute of Radioengineering and Electronics (IRE), RAS in November and December 2010,

I B Esipov Gubkin Russian Petroleum and Gas University, Moscow, Russian Federation, and the Andreev Acoustic Institute, Moscow, Russian Federation. E-mail: igor.esipov@mail.ru

Uspekhi Fizicheskikh Nauk **181** (11) 1228 – 1234 (2011)
DOI: 10.3367/UFNr.0181.201111m.1228
Translated by M N Sapozhnikov; edited by A Radzig

respectively. The most important achievements in 2010 pointed out at these sessions are discussed below. These achievements include:

(i) a new phenomenon of explosive instability and spatial localization of ultrasonic waves in ferromagnets;

(ii) an original method for metrology of nonlinear fields of ultrasonic focusing radiators in biological tissue;

(iii) experimental demonstration of the efficiency of coherent methods for the seismoacoustic sounding of the sea bottom.

In addition, it is important to highlight the development of a pilot parametric acoustic antenna for long-path ocean studies. The antenna was deployed in 2010, and now the first results of testing this new nonlinear acoustic device have been obtained.

Consider each of these results in more detail. The phenomenon of *the explosive instability of ultrasound in magnetics* has been demonstrated and studied by V L Preobrazhensky and coworkers at the International Laboratory of Nonlinear Magnetoacoustics of Condensed Media affiliated with the Scientific Center of Wave Studies, GPI RAS [1, 2].

The interaction of acoustic (elastic) vibrations with a nonlinear magnetic structure establishes conditions for the observation of strongly nonlinear acoustic phenomena in a solid. The specific features of nonlinear magnetoacoustic interaction in magnetics have been investigated for many years at Preobrazhensky's laboratory. The fact is that the coupling coefficient between magnetic and acoustic fields for certain types of acoustic vibrations in a number of magnetically ordered materials reaches a few dozen percent. In this case, the magnetic contribution to anharmonic (nonlinear) elastic moduli can be $\Delta C^{(3)} \approx (10^3 - 10^4) C^{(2)}$, where $C^{(2)}$ is the second-order elastic modulus. Such a strong effective anharmonicity, considerably exceeding the intrinsic anharmonicity of a crystalline lattice, was called the giant anharmonicity [3]. Under such conditions, higher-order nonlinear effects are distinctly manifested. In this case, the introduced nonlinearity strongly depends on an external magnetic field.

The modulation of the third-order nonlinearity by an alternate magnetic field can provide efficient three-phonon parametric excitation. The above-threshold dynamics of phonon triads qualitatively differs from the parametric generation of phonon pairs in magnetic media studied earlier, which was manifested, in particular, in the phase conjugation of ultrasound with giant amplification [4, 5]. Theoretical studies and numerical simulations have shown that the above-threshold three-phonon interaction with the electromagnetic pump field in magnetically ordered media is accompanied by the development of explosive instability and the spatial localization of ultrasonic waves. Figure 1 demonstrates the results of numerical simulations of the explosive amplification of a traveling wave in an antiferromagnet [6]. Explosive instability was observed in experiments upon the excitation of α-Fe_2O_3 [1] and $FeBO_3$ [2] antiferromagnetic single crystals by two successive electromagnetic pulses. The first pulse, with the harmonic carrier corresponding to the natural frequency of the crystal, produced initial acoustic perturbations. Then, a pump pulse at the tripled frequency followed. The phase of this pulse was changed according to the law providing a singular increase in the intensity of elastic ultrasonic vibrations [1]. Experimental results presented in Fig. 2 show that the special phase modulation of the electromagnetic pump leads to the suppression of the phase mechanism of nonlinear restriction of the amplitude of generated waves, and establishes conditions for the explosive above-threshold dynamics of three-phonon excitations.

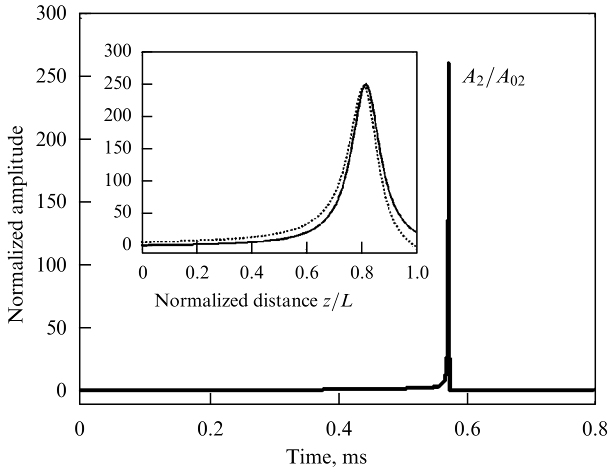

Figure 1. Time evolution of the explosive amplification of a traveling wave in a three-photon parametric process. The inset shows the spatial localization of the interacting waves. The solid curve corresponds to forward waves, and the dotted curve defines the backward wave.

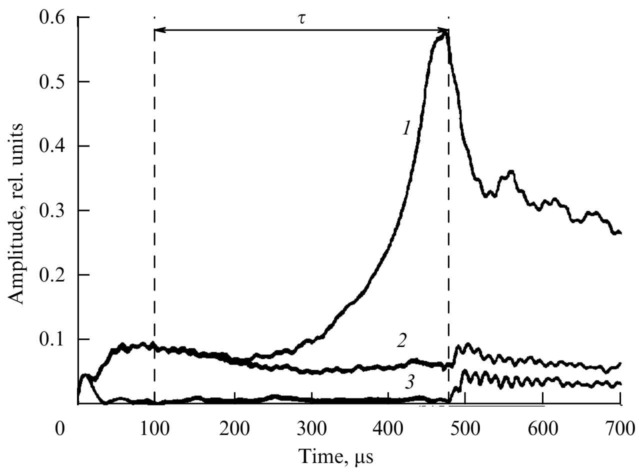

Figure 2. Experimental time dependence of the amplitude of magnetoacoustic vibrations at frequency ω upon transverse pumping of an α-Fe_2O_3 crystal by electromagnetic radiation at frequency 3ω with phase modulation of the pump (curve *1*), in the absence of pump modulation (curve *2*), and in the absence of the initial acoustic perturbation (curve *3*); τ is the pump pulse duration [5].

Among the most important results obtained in the field of physical ultrasound, investigations of processes of *high-intensity focused ultrasound* (HIFU) were pointed out in connection with the possibility of their applications in noninvasive surgery. The results in this field were obtained at the Chair of Acoustics, Physics Department at Moscow State University.

The use of HIFU for the local heating and destruction of tissue without the usual surgical invasion and the damage of surrounding tissues is a rapidly developing medical technology [7]. The destruction of tissue irradiated by HIFU is caused by the absorption of the ultrasonic energy in the tissue, resulting in its heating, followed by the necrosis of cells inside the irradiated tissue volume. Thermal effects are often accompanied by mechanical damage to the tissue, which is caused by bubbles produced under the effect of ultrasound. Recently, interest in the use of new procedures for the mechanical destruction (emulsification) of tissues without thermal coagulation has been increasing.

The Chair of Acoustics in the Physics Department at Moscow State University is a leading Russian scientific center in the field of studies of physical processes initiated by high-power focused ultrasound in biological tissues. Investigations in this area are performed in close collaboration with other institutions and laboratories in Russia, the main therapeutic-ultrasound scientific centers in the USA and Europe, the manufacturers of HIFU equipment, and metrological institutes in different countries.

One of the important areas in the development of HIFU technologies is the use of nonlinear acoustic phenomena for increasing the efficiency of thermal action on tissues and producing new nonthermal biological effects. The radiation intensity at the focus of HIFU sources reached a few dozen kilowatts per cm^2, nonlinear effects leading to the formation of shock fronts (discontinuities) in the wave profile with amplitudes of up to 60–100 MPa. It is well known that the energy absorption of a nonlinear acoustic wave containing discontinuities principally differs from the energy absorption of harmonic waves. The energy absorption of a harmonic wave is proportional to the square of its amplitude, whereas the absorption of a discontinuous wave is proportional to the cube of the discontinuity amplitude. As a result, the efficiency of heating a medium by discontinuous waves can increase by a few dozen and even hundreds of times. In addition, shock waves are focused on a smaller volume, thereby increasing the action locality. HIFU irradiation in the discontinuous-wave mode produces rapid localized tissue heating and boiling for a few milliseconds, opening new possibilities for the development of HIFU technologies [8, 9].

Researchers at Moscow State University have proposed the control of nonlinear effects by utilizing the repetitively pulsed operation mode of HIFU radiators with the same time-averaged intensity, but different peak pressures and period-to-pulse duration ratios [9]. It has been shown in experiments performed in collaboration with the Center of Industrial and Medical Ultrasound (CIMU APL) in Seattle that this method can provide principally different actions in tissues [9]. Thus, during continuous irradiation of liver tissue by ultrasonic waves with a small initial amplitude (Fig. 3a), the wave at the focus is harmonic and produces a small thermal necrosis locus which is clearly observed in the tissue section in the focal plane (white region). As the initial wave amplitude is increased (Fig. 3b), the wave shape at the focus is distorted and the heating efficiency enhances, which can lead to an unexpected radically new effect of the acoustic action on biological tissue. It was found that if a tissue boils periodically at the end of each pulse, a purely mechanical destruction (emulsification) of the tissue without thermal necrosis becomes possible (Fig. 3b). Finally, if the initial-wave and discontinuity amplitudes at the focus are very large and boiling occurs for a longer time during each of the pulses, the damage is observed in the form of a cavity surrounded by a thermal necrosis zone (Fig. 3c). Thus, ultrasonic waves with the same average intensities can produce tissue damage with different morphologies and sizes.

It should be noted that until recently just the time-averaged radiation intensity was employed as the main characteristic of HIFU irradiation. The results presented above reveal that, to predict adequately the expected effects, a considerably greater number of parameters of the ultrasonic field are required. New methods in the metrology of ultrasonic fields produced by HIFU radiators [10], which were developed by researchers at the Chair of Acoustics in collaboration with the Center of Industrial and Medical Ultrasound in Seattle, and measurements of the parameters of a nonlinear field in biological tissues from experimental data or simulations in water [11] were used by the International Electrotechnical Commission in the development of the first International Ultrasonic Standard in surgery.

An interesting HIFU application concerns the development of irradiation methods in which acoustic obstacles are located between a radiator and the focus. These obstacles are first and foremost bones, in particular, thoracic bones which complicate the fulfillment of ultrasonic surgical operations, for example, on the liver or heart (Fig. 4). The presence of strongly reflecting or strongly absorbing acoustic obstacles in organism tissue significantly restricts more widespread clinical HIFU applications. The absorption of ultrasound in

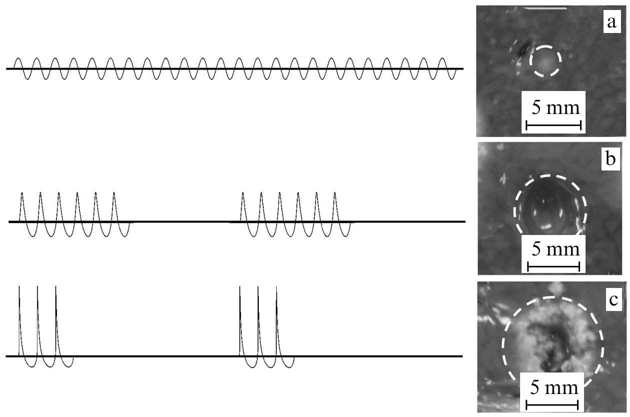

Figure 3. Profiles of an ultrasonic wave at the focus of an HIFU source and the corresponding types of tissue damage caused by repetitively pulsed HIFU irradiation.

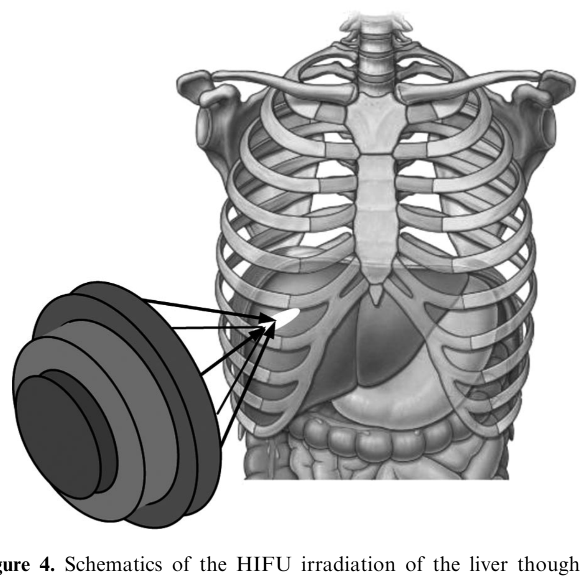

Figure 4. Schematics of the HIFU irradiation of the liver though the thorax. The main side effect of the operation reduces to overheating of the ribs and overlying tissue, including skin, caused by the strong absorption of ultrasound in the bones and its reflection from the bones.

bones is an order of magnitude higher than that in soft tissues. Acoustic impedances also strongly differ, resulting in the reflection of the ultrasonic energy from ribs. Another complication consists in a drastic decrease in the intensity of focused ultrasonic radiation caused by the same reason, which can become insufficient to damage tissues located behind the thorax. Recent experimental data give evidence that during direct irradiation of the liver through the thorax, ribs, and skin are heated even more strongly than tissue in the focal area. Of course, this is not admissible.

This problem was solved after the development of high-power two-dimensional phased therapeutic lattices and the elaboration of new HIFU irradiation protocols. Researchers of the Chair of Acoustics, Physics Department at Moscow State University, in collaboration with researchers at the Andreev Acoustic Institute, as well as the Imperial College and the National Physical Laboratory (NPL) in Great Britain, have developed and trialed a new method minimizing the action of ultrasound on ribs and preserving the high radiation intensity at the focus during irradiation of the liver [12, 13]. The method in the simplest version is based on the detachment of the lattice elements facing the ribs, so that ultrasound is transmitted to the focal spot mainly through intercostal gaps. The more complex modification of this method uses specially synthesized amplitude and phase field distributions over lattice elements, permitting to weaken diffraction effects during the propagation of ultrasound through the thorax, thus providing an electron scan of the focal point and constructing the configuration from several foci.

The operating capacity of the method has been confirmed in a joint experiment performed at the NPL. A lattice 170 mm in diameter with the radius of curvature of 130 mm, consisting of 254 elements 7 mm in diameter at a frequency of 1 MHz was used [12]. The possibility of a local damage to tissues located behind thoracic bones was demonstrated *in vitro*. In this case, the classical diffraction effect predicted theoretically was observed: two secondary maxima appeared in the focal plane behind the ribs along with the main focus. The mechanism of this effect is based on the interference of ultrasonic waves from two or more spatially separated sources which are intercostal gaps [14]. In this case, three corresponding areas of damage are produced in the tissue, which should be taken into account in the development of clinical protocols. These studies have given new data on the mechanisms of effects appearing during the propagation of HIFU through acoustic obstacles and provided the quantitative estimates of the focus splitting effect, which is important for practical implementations. The data obtained demonstrate the principal possibility of the application of this method in clinics for the destruction of tissues located behind thoracic bones without the overheating of bones and overlying tissue.

Experimental demonstration of the efficiency of coherent methods for seismoacoustic sounding of the sea bottom. The standard, modern, seismic, sea prospecting approach to determining the profile of an inhomogeneous bottom structure containing numerous reflecting layers is based on the use of incoherent pulsed sources (as a rule, pneumatic guns or sparkers) and extended receiving antenna systems (seismic braids). High-power pneumatic guns provide the signal level in the low-frequency range (down to 100 Hz), which, taking into account the directivity of the extended receiving antenna, is sufficient for achieving the required sounding depths (up to several kilometers). The spatial resolution of the method with such radiators can be improved by decreasing the signal duration, which is bounded from below by the design of the setup and is no less than ≈ 10 ms, which for the characteristic speed of sound in bottom deposits provides a resolution of about several dozen meters.

The application of coherent methods in seismic investigations offers a number of advantages related, first of all, to the possibility of using a prolonged coherent accumulation of received signals [15–17]. In this case, so-called complex signals, broadband modulated signals with a large base (the product of the pulse duration T by its spectral width F), are most interesting for practical implementations. Such signals are known to possess an autocorrelation function with the characteristic width of the main maximum smaller than the signal duration by a factor of FT ($FT \gg 1$). This means that, after the convolution of the received signal with the reference radiation, almost all the power of this signal is concentrated in the narrow maximum of the correlation function, which is in fact equivalent to a short pulse, but with a considerably higher emitted power (FT times higher). In addition, if the repeatability of signals is good enough, the energy of a long train of signals can be coherently accumulated, which also increases the sounding depth. As a result, the emitted signal power can be considerably reduced to provide the required sounding efficiency — the depth and (or) contrast of the structure of the bottom layers under study. Moreover, this energy gain allows one to consider the possibility of using high-frequency signals (up to ≈ 1 kHz) for seismoacoustic sounding. The application of high-frequency signals establishes conditions for a higher spatial resolution and considerably simplifies the technical realization of the system as a whole.

It should be emphasized that the peculiarities of the coherent approach are in no way specific for marine seismography. On the contrary, they are widely used in radiophysical methods for sounding inhomogeneous media. However, sources emitting signals with coherent properties sufficient for practical demonstration of the above-mentioned advantages are not employed in marine seismic prospecting at present.

In the last two decades, researchers at the Institute of Applied Physics (IAP), RAS have developed a number of high-power hydroacoustic sources emitting highly stable and well-controllable signals in the frequency range from a few hundred hertz to a few kilohertz, including broadband complex signals. This has opened up the real possibility for developing a coherent approach to seismic prospecting of the sea bottom. The commonly used in this situation signals are either linearly frequency-modulated (LFM) or phase-modulated (so-called pseudorandom). These signals provide approximately the same spatial resolution, and by using computer-controlled radiators, one or another regime of the signal formation can be realized. The stability of the sources themselves is limited only by the technical parameters of the master oscillators. Due to the digital control of radiation, any of the possible coherent approaches can be realized, namely: the matched filtration and convolution with the reference signal, the long accumulation of a train of signals, and the synthesis of an extended aperture by a single receiver (signal accumulation through a space coordinate) and the corresponding formation of its directivity.

Researchers at the IAP, RAS and the Institute of Oceanology, RAS have performed a number of joint

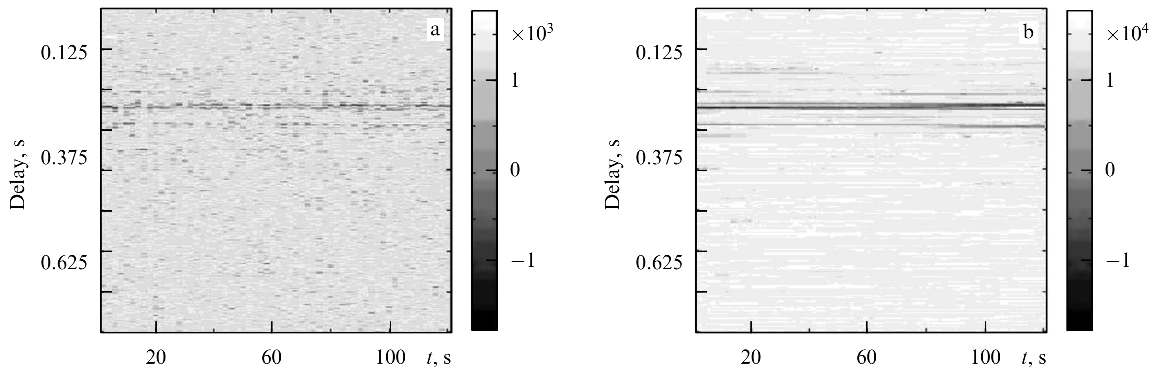

Figure 5. Portions of a seismogram corresponding to an individual bottom layer, obtained without the coherent accumulation of a train of pulses (a) and with the accumulation of a train of 16 coherent pulses (b). The time delay interval of 0–1000 ms corresponds to a depth of up to $\approx$ 1000 m.

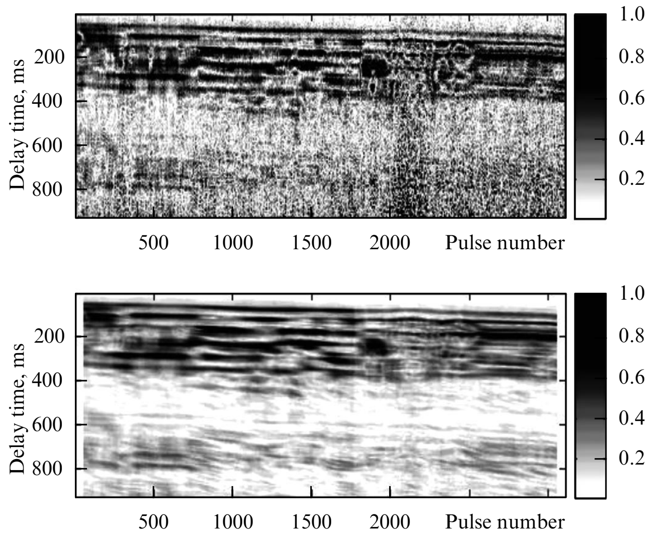

Figure 6. Seismograms obtained after sounding sea depth by LFM signals in the frequency band 180–230 Hz without interpulse accumulation (a) and by using the adaptive path accumulation of a train of up to 100 pulses (b).

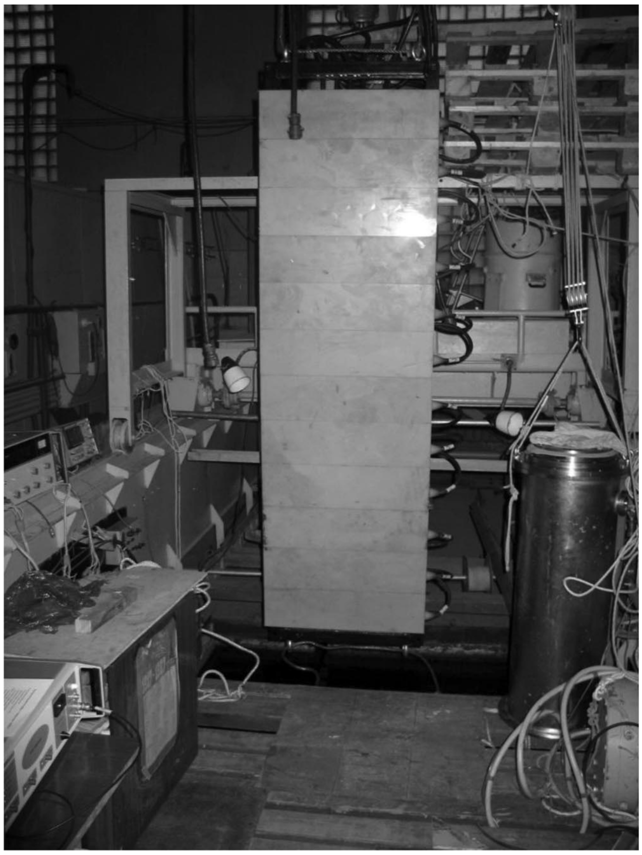

Figure 7. Parametric antenna before tests in a hydroacoustic pool.

experiments in the Caspian Sea, demonstrating the possibilities of coherent methods in marine seismoacoustics [18]. Hydroacoustic radiators were used, which generated synchronized trains of LFM pulses in different frequency bands ($\approx 50-100$ Hz) within a broad range ($\approx 100-1000$ Hz); the maximum radiation intensity of about 130 W was emitted in the frequency band from 180 to 230 Hz. The ultrasonic radiation was detected with a seismic braid consisting of 25 in-phase hydrophones. The coherent processing of received signals (reflected from bottom layers) included the matched filtration of individual pulses (convolution with the reference signal) and accumulation of a train of signals. The accumulation duration was limited by variations in the submersion depth of the radiator and variations in the bottom structure. The possibility of the coherent accumulation of a train of pulses reflected from bottom layers under particular experimental conditions was limited to the interval of $\approx 100-200$ s for the towing of a hydroacoustic radiator at the rate of three knots. This allowed efficient accumulation of up to a few dozen pulses (≈ 30). To improve the reconstruction quality of the bottom structure, a method was developed for accumulating pulses in paths in layers, taking into account the slopes of individual reflecting layers, which provided not only an increase in the number of pulses in the coherent train (up to a few hundred in practice) but also allowed adaptively estimating these slopes. Notice that most of the received signals had low noise stability (the signal-to-noise ratio was no more than 5 dB). However, the advantage in the signal-to-noise ratio after coherent signal processing reached 30 dB, which permitted the determination of the structure of bottom layers at depths of up to approximately 1000 m.

Figures 5 and 6 demonstrate the results of sounding a bottom structure along one of the paths. Fragments of the structure containing weakly contrasting layers were revealed

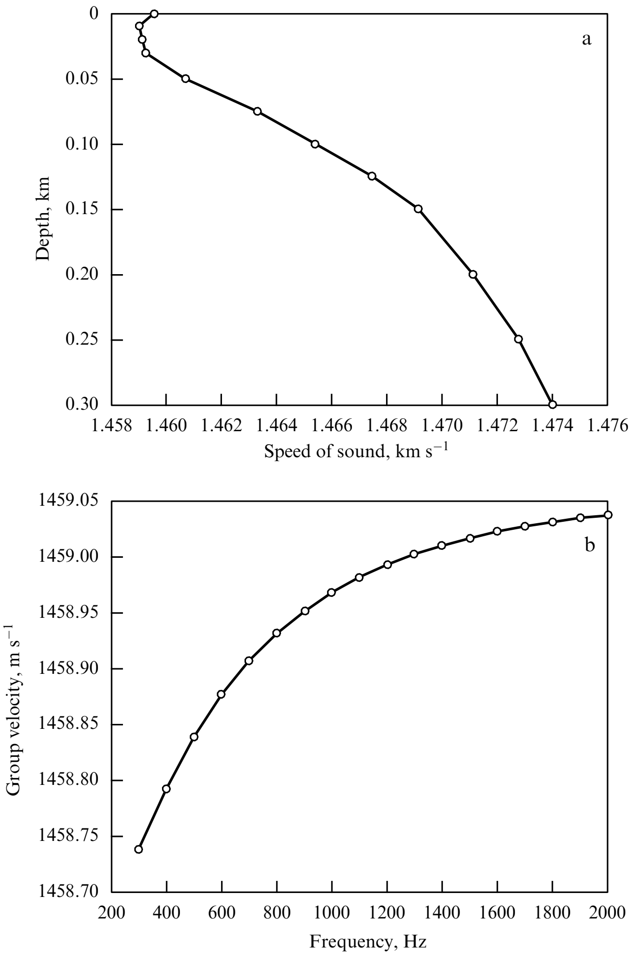

Figure 8. (a) Profile of the speed of sound in the Black Sea in February–March. (b) Frequency dependence of the group velocity of the first mode corresponding to the profile in Fig. 8a.

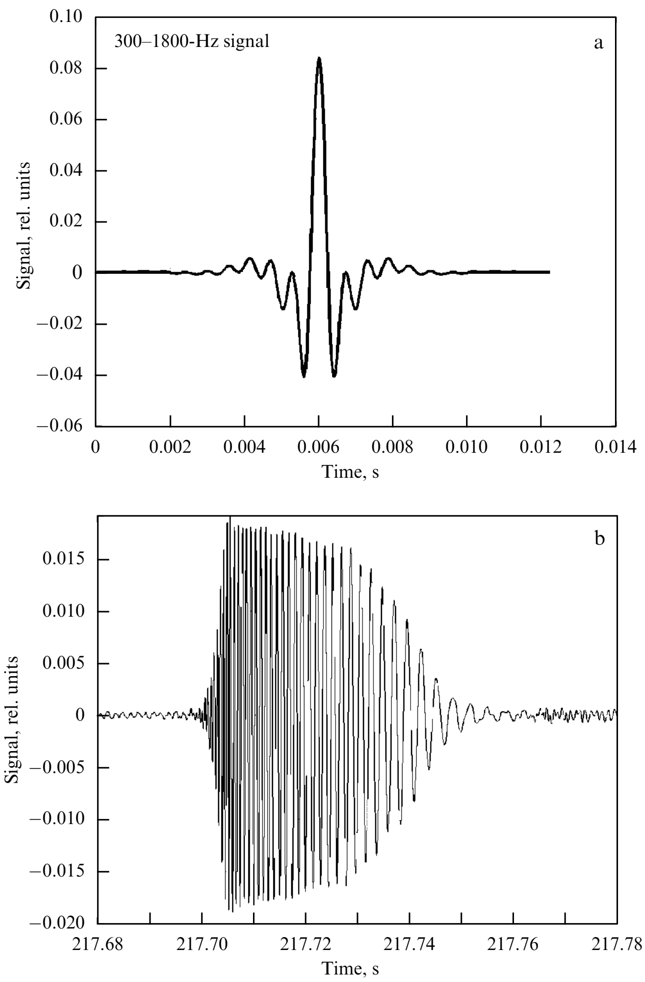

Figure 9. Influence of the frequency dispersion on the propagation of an acoustic signal in a Black Sea waveguide (Fig. 8a). (a) Pulse in the frequency band from 300 to 1800 Hz. (b) Same pulse at a distance of 318 km: first, high frequencies propagate, and then the low frequencies; the pulse duration at this distance is about 50 ms.

after the accumulation of trains consisting of up to 100 pulses. At the same time, only the autocorrelation compression of individual pulses did not provide a noticeable contrast in the case of a relatively small (≈ 10) base of LFM signals used in the experiments. The latters have shown that the seismo-acoustic sounding of the sea bottom structure at depths of up to ≈ 1000 m with high spatial resolution can be performed by using comparatively low-power (≈ 100 W) high-frequency (up to a few hundred hertz) coherent hydroacoustic sources.

Development of a pilot parametric acoustic antenna for ocean studies. Researchers at the Andreev Acoustic Institute and the Taganrog Technological Institute, South Federal University have developed a parametric antenna for monitoring sea areas at long paths and constructed a pilot. This work was performed within the framework of a project of the International Scientific and Technological Center and was supported by the European Union. A specific feature of this hydroacoustic antenna, operating on the principles of nonlinear acoustics, is the extremely narrow directivity diagram for low-frequency acoustic signals. The width of the diagram for the parametric antenna is almost constant in a broad frequency range. A sounding signal is formed in the sea medium, which is excited by the high-power, high-frequency intensity-modulated acoustic pump. The high-frequency pump is detected due to nonlinear interaction and a traveling-wave antenna is formed in the sea medium, which generates a sharply directed acoustic signal at the modulation frequency. Such a low-frequency acoustic signal emitted parametrically will further propagate in the sea depth independently of the high-frequency pump. Due to the nonresonance method of low-frequency signal generation, the parametric antenna emits sounding signals in an extremely broad frequency band (more than two octaves). Therefore, the realization of this project will allow the testing of a principally new emitting nonlinear-acoustic system for long-path sounding of sea areas and the ocean. This acoustic system (Fig. 7) has a comparatively small size (the emitting aperture size is 0.7×2 m^2), a broad signal frequency band (300–3000 Hz), and a high radiation directivity (no worse than 2° in the vertical plane) in the entire frequency range. These characteristics allow a good matching between directed parametric radiation and a waveguide structure in the sea.

At present, this antenna is being tested in the water area of the Sukhumi Hydrophysical Institute in Abkhaziya. The calculated characteristics of the parametric antenna should provide single-mode excitation of a sea waveguide efficient for monitoring the Black Sea or ocean investigations at distances of up to 1000 km. Notice that the possibility of applying a parametric antenna for long-path ocean studies was first demonstrated almost 20 years ago [19, 20].

The obtained characteristics of this parametric antenna allow studying the frequency dispersion during the propagation of an acoustic signal in a sea waveguide. Figure 8a displays the depth distribution of the sound speed typical for the Black Sea in the spring. This distribution causes changes in the propagation velocity of signals at different frequencies. The frequency dependence of the group velocity for the first mode of this waveguide is plotted in Fig. 8b. One can see from this figure that the dispersion during the propagation of a broadband signal in the frequency range lower than 2 kHz can be noticeable. Figure 9 shows the influence of this dispersion on the propagation of an acoustic signal in a Black Sea waveguide in the frequency band from 300 to 1800 Hz. One can see that, due to dispersion, the signal duration under these conditions changes by a factor of almost 25 along with the corresponding change in the signal intensity. This effect will be more pronounced at longer paths. Preliminary experimental studies of the propagation of acoustic radiation from a parametric antenna in a shallow-water waveguide [21] have revealed that, if the frequency modulation is matched with the waveguide, the duration of the emitted signal decreases, resulting in an increase in the signal-to-noise ratio and, hence, in the efficiency of acoustic means in a sea waveguide.

Thus, this new tool for ocean investigations establishes conditions for the selective excitation of modes in a broad frequency range, which in turn opens up the possibility of studying a new ocean characteristic — the frequency dispersion of signals in a waveguide. The study of this characteristic will complement our knowledge about the propagation of acoustic signals in ocean waveguide structures.

References

1. Preobrazhensky V et al. *J. Magn. Magn. Mater.* **322** 585 (2010)
2. Yevstafyev O et al. *J. Magn. Magn. Mater.* **323** 1568 (2011)
3. Ozhogin V I, Preobrazhenskii V L *Usp. Fiz. Nauk* **155** 593 (1988) [*Sov. Phys. Usp.* **31** 713 (1988)]
4. Brysev A P, Krutyanskii L M, Preobrazhenskii V L *Usp. Fiz. Nauk* **168** 877 (1998) [*Phys. Usp.* **41** 793 (1998)]
5. Preobrazhenskii V L *Usp. Fiz. Nauk* **176** 108 (2006) [*Phys. Usp.* **49** 98 (2006)]
6. Preobrazhensky V, Bou Matar O, Pernod P *Phys. Rev. E* **78** 046603 (2008)
7. Khokhlova V A *Programma Mezhdunarodnogo Onkologicheskogo Nauchno-obrazovatel'nogo Foruma ONKOKHIRURGIYA-2010 "V Budushchee cherez Novye Tekhnologii"* (Program of the International Oncological Scientific and Educational Forum 'Oncology Surgery-2010: To the Future through New Technologies', Moscow, May 31–June 2, 2010) p. 7; http://www.oncology.ru/events/2010/05/31/program/program.pdf
8. Canney M S et al. *Ultrasound Med. Biol.* **36** 250 (2010)
9. Canney M S et al. *J. Acoust. Soc. Am.* **127** 1760 (2010)
10. Kreider W et al., in *2nd Intern. MRgFUS Symp.: Current and Future Applications of MR-guided Focused Ultrasound, October 17–20, 2010, Washington, DC, USA*, p. 79
11. Bessonova O V et al. *Akust. Zh.* **56** 380 (2010) [*Acoust. Phys.* **56** 354 (2010)]
12. Bobkova S et al. *Ultrasound Med. Biol.* **36** 888 (2010)
13. Gavrilov L R et al. *Meditsin. Fiz.* (3(47)) 53 (2010)
14. Khokhlova V A, Bobkova S M, Gavrilov L R *Akust. Zh.* **56** 622 (2010) [*Acoust. Phys.* **56** 665 (2010)]
15. Lebedev A V, Malekhanov A I *Izv. Vyssh. Uchebn. Zaved. Radiofiz.* **46** 579 (2003) [*Radiophys. Quantum Electron.* **46** 523 (2003)]
16. Averbakh V S et al. *Akust. Zh.* **45** 5 (1999) [*Acoust. Phys.* **45** 1 (1999)]
17. Averbakh V S et al., in *Fundamental'nye Issledovaniya Okeanov i Morei* (Fundamental Studies of Oceans and Seas) Vol. 2 (Ed.-in-Chief N P Laverov) (Moscow: Nauka, 2006) p. 500
18. Lazarev V A et al. *Akust. Zh.* (in press)
19. Esipov I B et al. *Akust. Zh.* **39** 173 (1993) [*Acoust. Phys.* **39** 89 (1993)]
20. Esipov I B et al. *Akust. Zh.* **40** 71 (1994) [*Acoust. Phys.* **40** 61 (1994)]
21. Esipov I B et al. *Akust. Zh.* **55** 56 (2009) [*Acoust. Phys.* **55** 76 (2009)]